Structure, variability, and salt flux in a strongly forced salt wedge estuary

David K. Ralston,[1] W. Rockwell Geyer,[1] and James A. Lerczak[2]

[1] The tidally varying circulation, stratification, and salt flux mechanisms are investigated in a shallow salt wedge estuary where fluvial and tidal velocities are large and the steady baroclinic circulation is comparatively weak. The study integrates field observations and numerical simulations of the Merrimack River estuary. At moderate to high discharge the estuary is short and highly stratified, while at lower discharges it shifts to a longer, more weakly stratified estuary; the transition occurs when the length of the salinity intrusion is similar to the tidal excursion. The Merrimack is highly variable at tidal time scales owing to the advection and mixing of a bottom salinity front. Salt flux is predominantly due to tidal processes rather than steady baroclinic or bathymetric shear. Tidal pumping is important near the mouth, but inside the estuary salt flux is due to tidal asymmetries in the elevation and thickness of the halocline that depend on the tidal amplitude and river discharge. Conditions in the Merrimack, including the salinity intrusion length and stratification, vary more with event to seasonal shifts in river discharge than with spring-neap changes in tidal amplitude. An unstructured grid hydrodynamic model is used to simulate conditions in the Merrimack and model results are compared quantitatively against field observations. The model achieves a high skill against time series of water level, salinity, and velocity and captures the spatial structures of salinity, velocity, and salt flux observed in along- and across-estuary transects. High model skills depend on accurate and well-resolved grid bathymetry and low background vertical and horizontal diffusivities.

1. Introduction

[2] Estuarine conditions depend on fluvial, tidal, and baroclinic forcing. The river supplies a mean volume flux and a source of buoyancy, tidal oscillations generate currents and a source of turbulent mixing, and the density gradient between fresh and salt water drives baroclinic circulation. The relative balance among these factors determines characteristics of an estuary such as the length of the salinity intrusion, stratification, and mechanisms of exchange and dispersion. In estuaries that are deep and have moderate river and tidal velocities, the baroclinic pressure gradient provides the dominant mechanism for creating residual circulation, stratification, and up-estuary salt flux. Physical processes in baroclinically dominated estuaries have been well documented, and examples include the James [*Pritchard*, 1952],

Delaware [*Garvine et al.*, 1992], and Hudson [*Lerczak et al.*, 2006] river estuaries and San Francisco Bay [*Stacey et al.*, 2001; *Monismith et al.*, 2002].

[3] In contrast, we consider the Merrimack River estuary, where river and tidal velocities are considerable and steady baroclinic circulation is comparatively weak. The Merrimack is a river on the northeastern coast of the United States, but it is representative of many estuaries that are relatively shallow with large tidal and freshwater velocities. Estuaries that are dynamically similar to the Merrimack include the Columbia [*Jay and Smith*, 1990b], Connecticut [*Garvine*, 1975], Fraser [*Geyer and Farmer*, 1989], and Snohomish [*Wang et al.*, 2009] river estuaries. Common characteristics are that they are short (i.e., the length of the salinity intrusion is similar to the tidal excursion), are strongly stratified, and have strong horizontal salinity gradients (i.e., bottom and/or surface fronts). Such short, strongly stratified systems have been termed salt wedge estuaries, but strong tidal velocities distinguish them from microtidal salt wedges such as the Mississippi, Rhone, and Ebre estuaries [*Keulegan*, 1966; *Ibanez et al.*, 1997], where tides do not significantly modify the estuarine structure and unsteadiness in river discharge is the principal source of time dependence.

---

[1]Woods Hole Oceanographic Institution, Woods Hole, Massachusetts, USA.
[2]College of Oceanic and Atmospheric Sciences, Oregon State University, Corvallis, Oregon, USA.
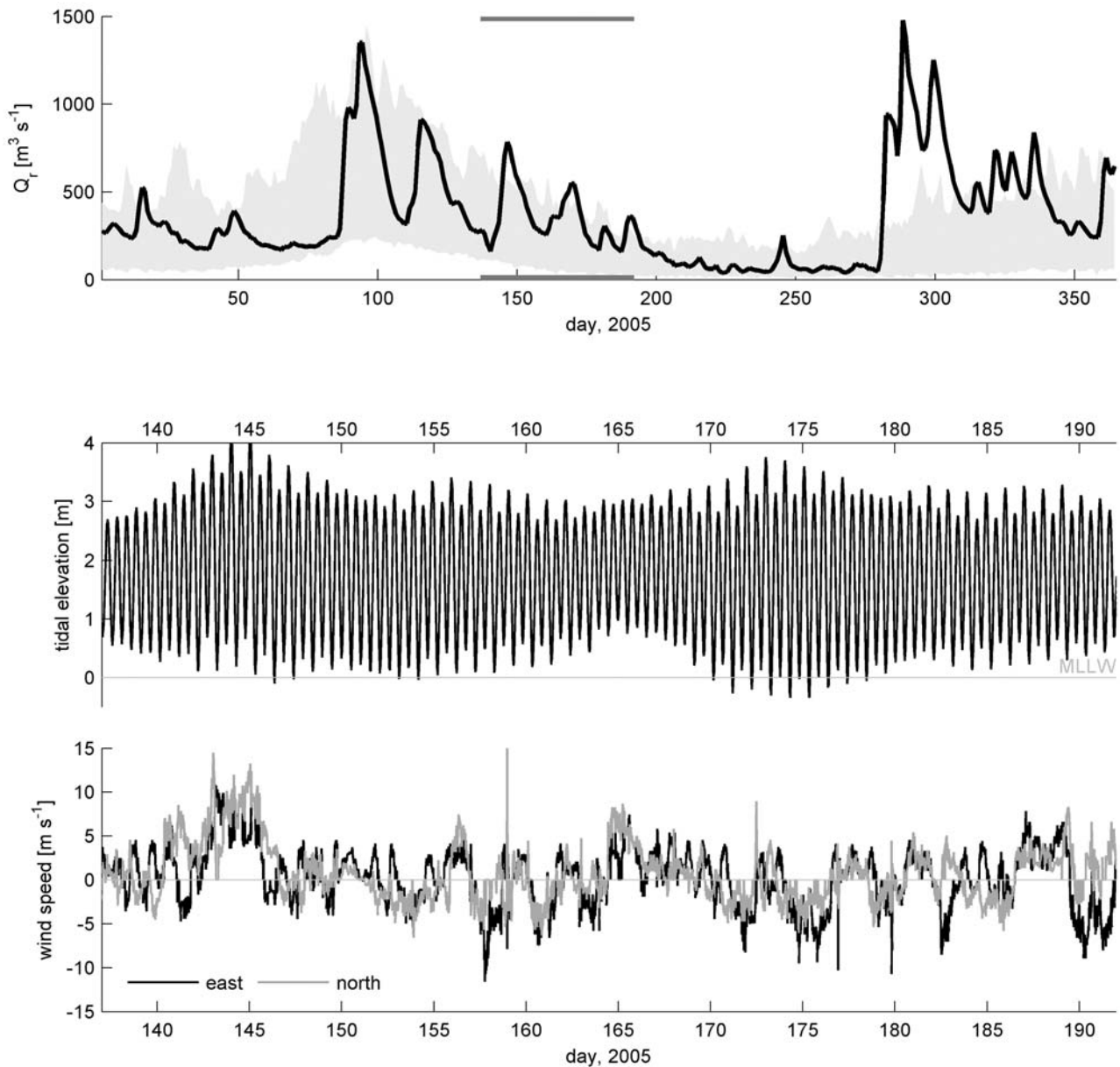
Figure 1. Forcing conditions during the observations. (top) River discharge (U.S. Geological Survey gage at Lowell), where the solid line is from 2005 and gray shading shows the seasonal variability of the 5th and 95th percentiles of discharge since 1924. Horizontal bars indicate the period of observations and are the axis limits of the lower two plots. (middle) Water level (National Oceanic and Atmospheric Administration tide gage at Boston). (bottom) East (black) and north (gray) wind (Plum Island station and regional airports).

[4] A primary objective of this work is to characterize the salinity distribution, circulation, and salt flux mechanisms in the Merrimack. In addition, shipboard and moored observations are used to evaluate simulations from an unstructured grid numerical model of the estuary and to identify the model attributes that were necessary to achieve high skill. Tidal and longer-term variability in the longitudinal and lateral structure of salinity and velocity in the estuary are described using observations and model results. The up-estuary salt flux is decomposed into steady and tidal components to quantify the dominant salt flux mechanisms, and a scaling is developed for the tidal dispersivity and

salinity intrusion length. To link results in the Merrimack to other estuaries, nondimensional scaling is used to illustrate the relative influence of river, tidal, and baroclinic forcing on stratification and salinity intrusion length.

2. Methods

2.1. Site Description

[5] The Merrimack River estuary is the fourth largest river in New England, with a mean discharge of 220 m^3 s^{-1} and an annual range from about 1500 m^3 s^{-1} during the spring freshet to less than 50 m^3 s^{-1} in late summer (Figure 1). The
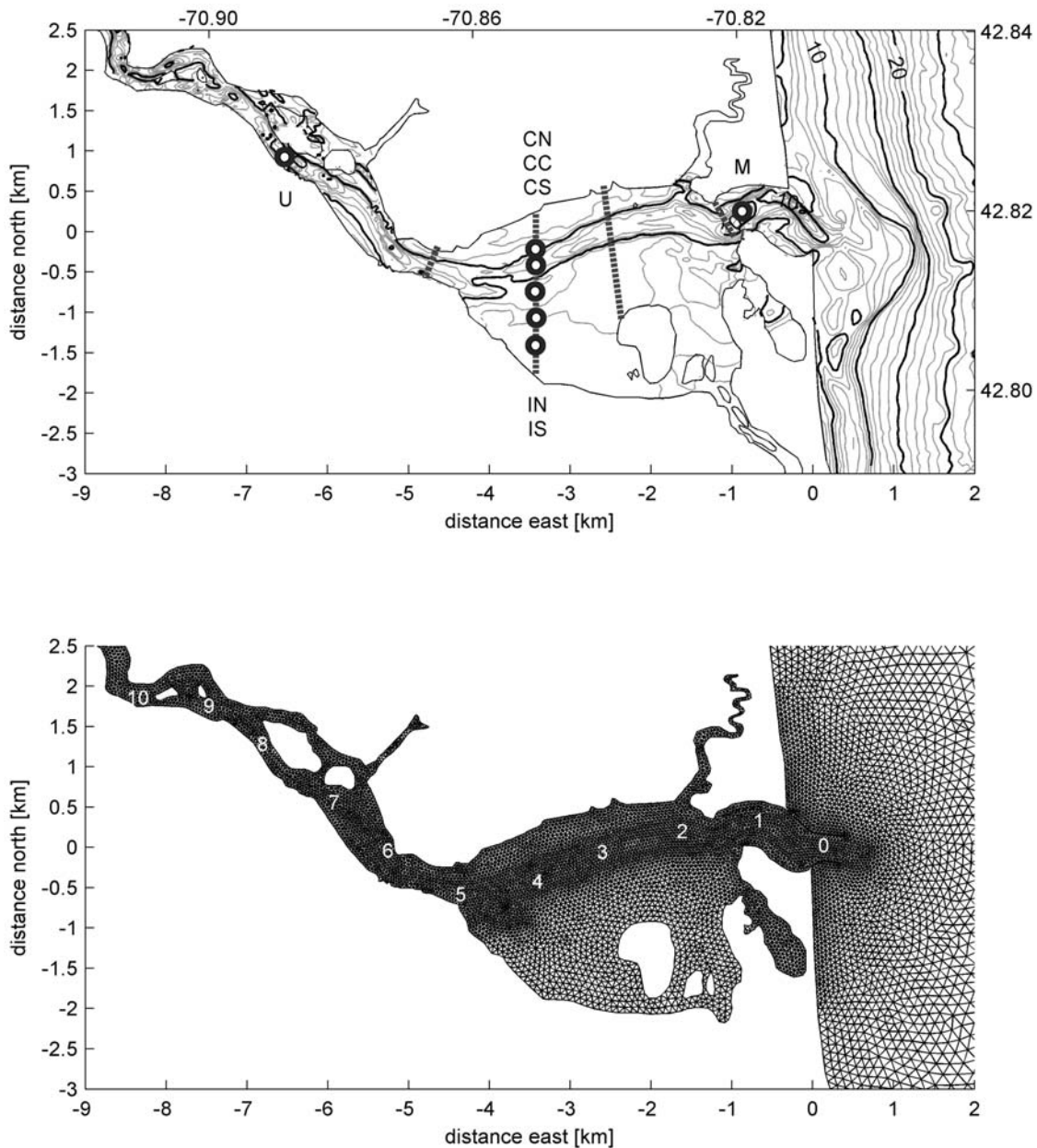
Figure 2. Bathymetry and model grid. (top) Bathymetry (contours every 1 m, darker contours every 5 m), with moored instruments shown by triangles and lines denoting location of cross-estuary transects for salinity flux measurements. Stations are located at the mouth (M), central north (CN), central channel (CC), central south (CS), intertidal north (IN), intertidal south (IS), and up-estuary (U). (bottom) Finite Volume Coastal Ocean Model (FVCOM) grid, with distance from the mouth along the channel thalweg indicated (km).

lower 35 km of the river is tidal, with a mean tidal range at the mouth of 2.5 m and spring tides of about 4 m. The channel of the upper estuary is narrow (200–500 m wide) and has a series of shallow sills (typical depths of 4 to 6 m) and deeper holes (typical depths of 8 to 10 m) (Figure 2). Between 1.5 and 5 km from the mouth the estuary opens into a broad embayment with intertidal flats and fringing salt marsh. The channel (5 to 10 m deep) near the mouth is narrow and constrained by rock jetties. A shallow ebb-tide bar (4 m deep) is located about 0.5 km offshore of the mouth.

2.2. Observations

[6] Observations with moored instruments and shipboard surveys were made in the spring and summer of 2005. Moorings were deployed in along- and across-channel arrays (Figure 2). Five moorings were spaced across the embayment mid estuary to measure lateral gradients in salinity and velocity. From north to south, the stations have been labeled central north (CN), central channel (CC), central south (CS), intertidal north (IN), and intertidal south (IS). Additional moorings were placed at the mouth (M) and

about 8 km up-estuary (U) to record along-channel gradients. Most moorings had acoustic Doppler current profilers (ADCPs) with near-surface and near-bed conductivity-temperature (CT) sensors. The northern intertidal frame had an ADCP and a near-bottom CT sensor, while the southern intertidal frame had only a bottom CT sensor. Pressure sensors were deployed on three frames along the main channel (M, CC, and U).

[7] The moored instruments collected data from 16 May to 12 July, with some data loss due to fouling. The conductivity cells on several of the near-bottom salinity sensors (M, CN, CC, and U) became clogged with sediment late in the deployment. To calculate salinities then we used the temperature-salinity relationship measured at working sensors and the temperatures observed at the sensors with fouled conductivity cells.

[8] In addition to the moorings, shipboard surveys were made using conductivity-temperature-depth data and ADCPs over semidiurnal tidal periods. Surveys included the along-channel salinity field, the lateral distribution of salinity and velocity at four cross sections (locations shown in Figure 2), and the salinity in the plume offshore. The shipboard surveys occurred during three periods with mean discharges of 250, 550, and 350 $m^3 s^{-1}$.

2.3. Numerical Model

[9] To complement the field observations, we have implemented a numerical model of the Merrimack using the Finite Volume Coastal Ocean Model (FVCOM) [*Chen et al.*, 2003, 2008]. FVCOM has a grid composed of triangular elements horizontally and σ layers vertically (Figure 2). Grid resolution varied from about 20 m inside the estuary, in regions with strong bathymetric gradients, to about 3000 m at the offshore boundary. The model domain extended 35 km offshore from the mouth to minimize boundary influences. FVCOM includes wetting and drying, and the minimum water depth for a cell to be active was set to 0.05 m. Twenty σ levels were used vertically. Ten levels did not sufficiently resolve the density structure in the estuary, but 30 levels produced results quantitatively similar to those with 20 levels.

[10] The model bathymetry was based on National Oceanic and Atmospheric Administration (NOAA) depth soundings but was augmented by water depths recorded during our hydrographic surveys. Bathymetric data from the surveys were necessary to resolve sharp gradients between the channel and the intertidal shoals mid estuary. Shear fronts were observed in the field at the channel/shoal interface during ebbs, and the model did not reproduce them until the sharp bathymetric gradient was incorporated in the model grid. The surveys were also important for establishing bathymetry on the intertidal flats, where NOAA soundings were sparse or nonexistent.

[11] Boundary conditions included tidal forcing offshore and river discharge. For simulations corresponding with the observation periods, the tidal record from the NOAA station at Boston (No. 8443970) was used to drive the offshore boundary water surface elevation. River discharge data from the U.S. Geological Survey (USGS) gage at Lowell (No. 01100000) was multiplied by 1.1 to account for inputs below the gauging station, based on watershed areas and data from stream gages on tributaries downstream of Lowell

(Spicket River, No. 01100561; Shawsheen River, No. 01100600; and East Meadow River, No. 01100700).

[12] For simulations corresponding with the observations, the offshore salinity boundary condition was based on data from the Gulf of Maine Ocean Observing System (GoMOOS). GoMOOS buoys in Massachusetts Bay (buoy A) and on the Western Maine Shelf (buoy B) are near the open boundary of the model domain, with measurements 1, 20, and 50 m below the surface. The depth-dependent, time-varying salinity at the open boundary was prescribed based on the buoy observations. The seasonal variability in Gulf of Maine salinity due to coastal freshwater input affected the salinity of water that advected into the Merrimack. Over the study period, the offshore salinity varied between about 30 and 32 practical salinity units (psu). Temperature was not included as a dynamic variable in the model because salinity dominated the density variability in the estuary and plume.

[13] Wind forcing was included in simulations of the observations. Wind data were from a meteorological station on the northern end of Plum Island, the barrier island between the Merrimack and the Gulf of Maine (data courtesy of WeatherFlow Inc.). During periods when the Plum Island station was unavailable, wind data came from airports at Lawrence, Massachusetts (National Climate Data Center WBAN 94723), and Portsmouth, New Hampshire (WBAN 04743). Among the nearby meteorological stations these stations correlated best with the Plum Island data during periods with simultaneous observations.

[14] FVCOM incorporates options for turbulence closure through the General Ocean Turbulence Model (GOTM). GOTM is a one-dimensional vertical module that recasts various closure schemes in a uniform format [*Umlauf and Burchard*, 2003]. The results presented here use the $k - \varepsilon$ turbulence closure [*Rodi*, 1987; *Canuto et al.*, 2001]. For the model to reproduce the strong pycnocline observed during high-discharge conditions, it was necessary to set the background turbulent diffusivity to a small value ($10^{-7} m^2 s^{-1}$). Similarly, the sub-grid-scale horizontal diffusivity was minimized to limit the nonphysical mixing of the sharp horizontal salinity gradient. FVCOM incorporates horizontal diffusivity closure, but in this study higher skills were achieved when the horizontal diffusivity was set to 0.

[15] For bulk properties like the salinity and velocity at the moorings, the model was not particularly sensitive to the choice between $k - \varepsilon$ and the Mellor-Yamada turbulence closure. The choice of $k - \varepsilon$ instead of Mellor-Yamada was based on comparisons of turbulence characteristics (buoyancy fluxes and Reynolds stresses) with observations from a different study in the Merrimack using an array of acoustic Doppler velocimeters and fast-response conductivity sensors. The turbulent mixing in the Merrimack and sensitivity to the closure scheme are discussed in detail in a companion manuscript (D. K. Ralston et al., Turbulent mixing in a strongly forced salt wedge estuary, submitted to *Journal of Geophysical Research*, 2010).

[16] The model was calibrated by adjusting the bottom roughness scale (z_0) to match the tidal advection of the salinity intrusion past the moored instruments. The results presented here use a constant, spatially uniform z_0 of 0.5 cm. A uniform z_0 is not ideal, as it does not reflect the spatial heterogeneity in size and composition of bottom roughness elements. In parts of the main channel the bed is composed

predominantly of coarse sand, and sand waves over 1 m in height can develop [*Hartwell*, 1970; *FitzGerald et al.*, 2002]. On the intertidal shoals, the bed is fine sand and mud and the bed forms are much smaller. Additionally, outcrops of bedrock occur at several locations along the main channel and introduce large-scale roughness. The spatial heterogeneity in bottom composition could be represented as a spatially variable z_0, but without bottom-type data a constant value was imposed.

[17] The value of z_0 is higher than reported in recent modeling studies of the Hudson River ($z_0 = 0.2$ cm [*Warner et al.*, 2005]), Chesapeake Bay ($z_0 = 0.05$ cm [*Li et al.*, 2005]), and Snohomish River ($z_0 = 0.025$–0.1 cm [*Wang et al.*, 2009]) estuaries. The relatively high friction required to match observations may compensate for roughness elements (e.g., sand waves, bedrock outcrops, and bridge abutments) that are not resolved in the model grid. In fact, an even larger z_0 of 2.0 cm yields better agreement with the arrival of the salinity intrusion at the up-estuary mooring, but the greater z_0 is inconsistent with advection of the salinity front across the intertidal flats and with the stratification observed at several stations. We also ran the model using a depth-dependent formulation for z_0, but it did not significantly improve the agreement with observations compared with a uniform z_0. The spatial heterogeneity in friction likely depends on more than water depth alone. While uncertainty remains in the spatial (and temporal) variability in the bottom roughness, it is important to note that the results shown here do not fundamentally change over a reasonable range of z_0.

[18] The model was run over the observation period from May to July 2005. Additional idealized simulations covered the parameter space of tidal and fluvial forcing with constant Q_r and M_2 tidal forcing. For the idealized simulations, discharge was varied over the seasonal range (25, 50, 100, 200, 400, 700, 1000, and 2000 m^3 s^{-1}) and the tide was varied over neap to spring amplitudes (2.0, 2.4, 2.8, and 3.2 m range). For moderate to high discharge (>100 m^3 s^{-1}) the estuary responded quickly and only a brief spin-up period (about four M_2 periods) was necessary to reach equilibrium. Similarly, during the observation period the model responded quickly to forcing changes and was insensitive to initial conditions.

2.4. Model Evaluation

[19] We used along- and across-channel surveys of salinity and velocity to assess the model results, including tidal variability in the salinity intrusion, degree of stratification, lateral flow structure, and frontal locations. We also evaluated the model quantitatively against the moored salinity and velocity time series using several skill metrics. The model skill score (SS) depends on the root-mean-square error between the model and observations normalized by the standard deviation of the observations:

$$\text{SS} = 1 - \frac{\sum_{i=1}^{N}(X_{\text{mod}} - X_{\text{obs}})^2}{\sum_{i=1}^{N}(X_{\text{obs}} - \overline{X}_{\text{obs}})^2} = 1 - \frac{1}{\sigma_{\text{obs}}^2}\frac{1}{N}\sum_{i=1}^{N}(X_{\text{mod}} - X_{\text{obs}})^2, \quad (1)$$

where X is the variable of interest and $\overline{X}$ is the time mean [*Murphy*, 1988]. The maximum SS is 1 when the model exactly agrees with the observations. An SS of 0 indicates that the model provides equal predictive skill as assuming the mean of the observations, and a negative SS indicates that the model is less predictive than the mean of the observations. Similar metrics for hydrodynamic and ecosystem models of the coastal ocean have been defined as an SS [*Oke et al.*, 2002], a model efficiency [*Allen et al.*, 2007], or a cost function (= 1 − SS) [*Friedrichs et al.*, 2007]. For reference, an evaluation of a hydrodynamic and ecosystem model in the southern North Sea categorized an SS > 0.65 as excellent, 0.5 to 0.65 as very good, 0.2 to 0.5 as good, and <0.2 as poor [*Allen et al.*, 2007].

[20] In addition to the SS, we calculate the correlation coefficient (r) between model and observations:

$$r = \frac{\sum_{i=1}^{N}(X_{\text{mod}} - \overline{X}_{\text{mod}})(X_{\text{obs}} - \overline{X}_{\text{obs}})}{\left[\sum_{i=1}^{N}(X_{\text{mod}} - \overline{X}_{\text{mod}})^2 \sum_{i=1}^{N}(X_{\text{obs}} - \overline{X}_{\text{obs}})^2\right]^{1/2}}$$

$$= \sigma_{\text{mod}}^{-1}\sigma_{\text{obs}}^{-1}\frac{1}{N}\sum_{i=1}^{N}(X_{\text{mod}} - \overline{X}_{\text{mod}})(X_{\text{obs}} - \overline{X}_{\text{obs}}). \quad (2)$$

The correlation coefficient (r) measures the linear relationship between the model and the observations. The SS (equation (1)) can be shown to depend on r and two additional terms:

$$\text{SS} = r^2 - \left(r - \frac{\sigma_{\text{mod}}}{\sigma_{\text{obs}}}\right)^2 - \left(\frac{\overline{X}_{\text{mod}} - \overline{X}_{\text{obsd}}}{\sigma_{\text{obs}}}\right)^2 \quad (3)$$

[*Murphy*, 1988]. The second term on the right-hand side of equation (3) represents the difference in variance between the model and the observations, and it vanishes when the slope of the linear regression is equal to 1; that is, the model correctly predicts the amplitude of the observed variations. The last term represents the mismatch between the mean of the model and the mean of the observations, and it corresponds to the intercept of the linear regression [*Murphy*, 1988]. The correlation coefficient (r) is greater than the SS except in the case of a linear regression with a slope equal to 1 and no mean model bias.

[21] Other estuarine modeling studies [*Li et al.*, 2005; *Warner et al.*, 2005] have defined model skill as

$$\text{SS}_W = 1 - \frac{\sum_{i=1}^{N}|X_{\text{mod}} - X_{\text{obs}}|^2}{\sum_{i=1}^{N}(|X_{\text{mod}} - \overline{X}_{\text{obs}}| + |X_{\text{obs}} - \overline{X}_{\text{obs}}|)} \quad (4)$$

[*Wilmott*, 1981]. We evaluated the model by this metric but found that it produced a narrow range of skill values and was not as sensitive to changes in model parameters as the SS. In most cases, the model skill according to equation (4) was greater than r. For example, if we compare two sets of
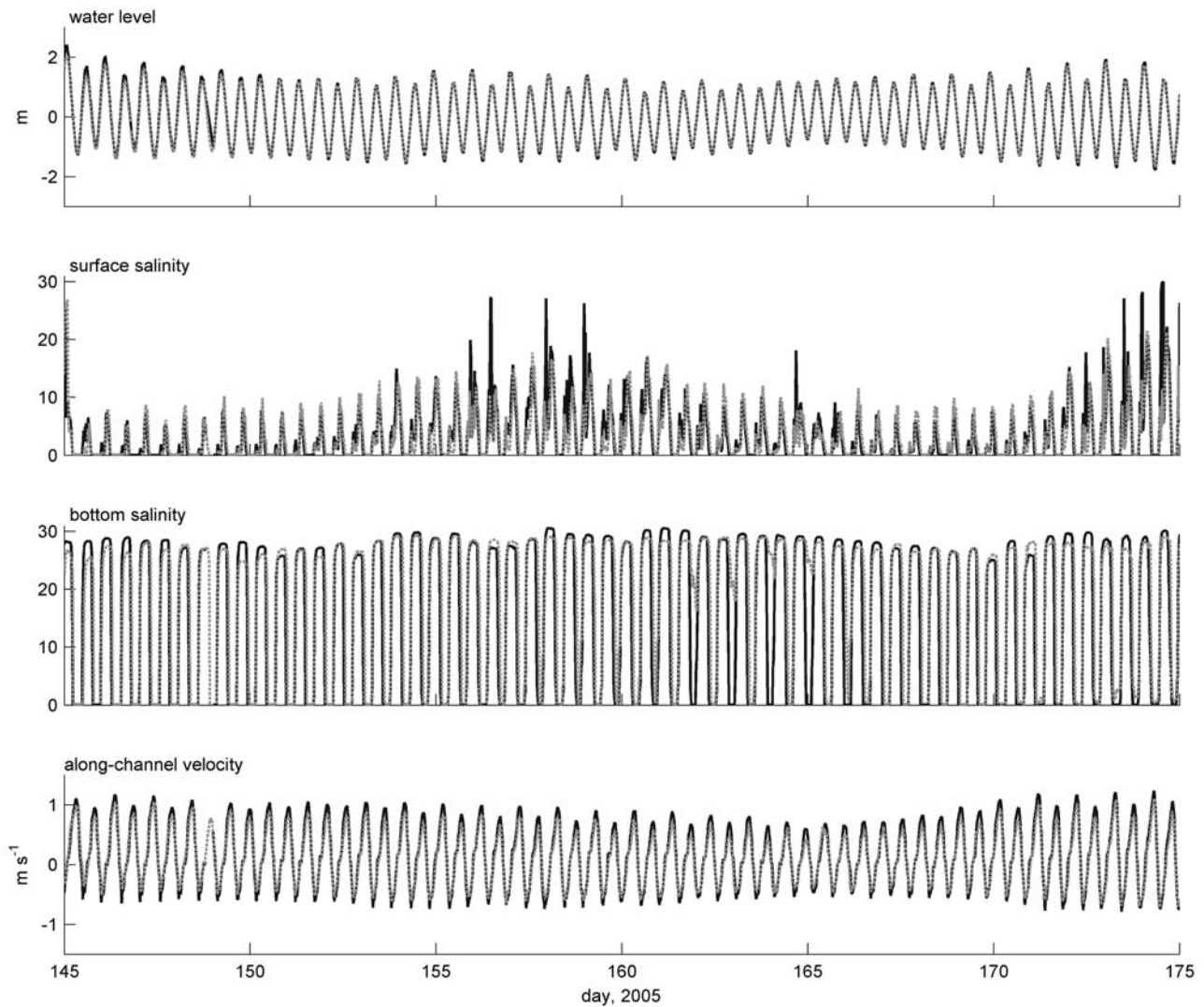
Figure 3. Observations (gray) and model results (black) at the central channel mooring. Water surface elevation, surface and bottom salinity, and depth-averaged along-channel velocity are shown.

randomly generated numbers between 0 and 1 (10^5 elements), we find that $r \approx 0.0$ (no correlation), SS ≈ -1.0 (no predictive skill), and $SS_W \approx 0.4$.

3. Results

[22] Observations and model results are presented together, with dual objectives: to evaluate the model skill and to characterize conditions in this type of estuary. Skill is assessed quantitatively using time series from moored observations of water surface elevation, surface and bottom salinity, and velocity profiles. The modeled and observed time series at the CC station are shown as an example (Figure 3), and similar results at the other stations are summarized in Table 1. Additional comparisons of the longitudinal and lateral distributions of salinity and velocity between the model and the observations are shown (Figures 5, 6, 7, and 8). The evaluations of estuarine structure provide a more integrative assessment of the model than the time series SSs. More importantly, the sections characterize key features of

circulation, stratification, and time dependence in shallow salt wedge estuaries.

3.1. Model Skill Assessment

3.1.1. Water Level

[23] At the four stations (M, CC, CS, and U) with measurements of water surface elevation, r values were greater than 0.99 (Table 1). SSs decreased with distance up-estuary, ranging from 0.92 at the mouth to 0.78 up-estuary. The lower skills at the up-estuary station may be due to inadequate resolution of the bathymetry at a channel constriction. Similar errors due to insufficient bathymetric resolution are seen in the velocity skill at the up-estuary station. The maximum absolute errors in water level occurred when regional metrological forcing created sea-level setup in the Gulf of Maine. Spatial gradients in the offshore water level were not incorporated into the uniform boundary forcing (e.g., days 143–147), and local wind effects were poorly captured by the sparse local meteorological data. This incomplete resolution of remote

Table 1. Skill Scores (SS) and Correlation Coefficients (*r*) from Comparison of Model with Observations in 2005

Location	Water Surface		Salinity (Bottom)		Salinity (Surface)		Velocity (Depth Avg.)		Velocity (Profile)	
	SS	*r*	SS	*r*	SS	*r*	SS	*r*	SS	*r*
Mouth	0.92	0.99	0.88	0.94	0.86	0.94	0.96	0.98	0.85	0.94
Central north	—	—	0.73	0.89	0.29	0.80	0.94	0.97	0.90	0.96
Central channel	0.86	0.99	0.70	0.88	0.40	0.77	0.96	0.99	0.88	0.98
Central south	0.85	0.99	0.90	0.96	0.74	0.87	0.95	0.97	0.88	0.96
Intertidal north	—	—	0.94	0.99	—	—	0.78	0.89	0.64	0.80
Intertidal south	—	—	0.92	0.99	—	—	—	—	—	—
Up-estuary	0.78	0.99	0.74	0.88	0.70	0.88	0.81	0.95	0.73	0.89

and meteorological forcing yielded lower skills for subtidal water surface elevations (average scores = 0.80) than for the tidal water surface (average SS = 0.86). Despite these limitations, the model generally captures the amplitude and phase of the barotropic tide in the estuary.

3.1.2. Salinity

[24] Bottom salinities were measured at all seven locations and surface salinities at all but the two intertidal stations. Bottom salinities ranged between nearly oceanic and completely fresh, and in many cases this variability occurred every tidal cycle. The effect of spring-neap tidal forcing on bottom salinity was most evident up-estuary. During spring tides the salt wedge moved farther upstream and high-salinity bottom water was observed at the up-estuary station for a longer fraction of the tidal cycle.

[25] The model achieves a high skill at predicting both the tidal propagation of the salt wedge and the development and breakdown of stratification. SSs for bottom salinity ranged between 0.70 and 0.94 (Table 1). The model captures not only the along-channel advection of the salinity intrusion, but also the lateral transport onto the intertidal shoals, where bottom salinity SSs were 0.94 (IN) and 0.92 (IS). SSs were generally lower for surface salinities than for bottom salinities, ranging between 0.29 and 0.86. The lowest surface SSs were mid estuary at CN (0.29) and CC (0.40), and scores at the other stations were all higher than 0.70. The low scores at CN and CC resulted from errors in the position of a surface tidal intrusion front (described in section 3.2.3). The salinity difference across the front was typically greater than 20 psu, so the error in salinity at the sensor was large if the position of the front was incorrect by as little as 100 m. The position of the surface front is likely sensitive to wind, and the wind conditions were not well resolved.

3.1.3. Velocity

[26] Velocity profiles were observed at six stations and were rotated into local along-channel and across-channel components by minimizing the variance of the vertically averaged current in the across-channel direction. Model velocities were rotated using the same rotation angles as the observations and were averaged over depth cells corresponding to the depths measured by the ADCPs. Overall, SSs for depth-averaged along-channel velocities were high, with the M, CN, CC, and CS stations all around 0.95 (Table 1). The SS at the intertidal station was the lowest (0.78). Flows on the shallow flats (typically <0.5 m) were less constrained to the along-channel direction and were more sensitive to wind, and the shallow ADCP measurements were noisier than at other stations. Skill was lower at the up-estuary station (0.81) than at other stations.

Maximum depth-averaged velocities observed during ebbs (around 1.2 m s^{-1}) at the up-estuary station were significantly greater than calculated in the model (around 0.7 m s^{-1}). The up-estuary mooring was at a constriction and bedrock outcrop, where the model grid and bathymetry may have been insufficiently resolved. An underresolved grid (30–40 m spacing in this region) would yield a smoother along-channel transition and widen a narrow channel. A wider channel in the model just upstream from the mooring is consistent with lower velocities in the model during ebbs, despite the relatively high SSs for water elevation and salinity at the same location.

[27] In addition to the depth-averaged along-channel velocities, we compare the model results with the velocity structure recorded by the ADCPs by summing the velocity data over time and depth. Overall, SSs for along-channel velocity profiles were less than for the depth averages but remained high. At the mouth and mid estuary moorings, the SSs ranged between 0.85 and 0.90. Skills were lower on the intertidal shoals (0.64) and up-estuary (0.73), for the reasons discussed previously. To illustrate the velocity structure we focus on three moorings across the channel mid estuary at selected times during the tidal cycle (Figure 4). The along-channel velocity profiles have been phase averaged relative to the M$_2$ tidal cycle over 3 days during moderate discharge conditions. The envelope of velocities shows variability over the 3 day period. These velocity profiles are representative but vary in detail with changes in discharge or tidal forcing. Note that the observed velocity profiles are truncated because ADCPs do not measure near-bottom or near-surface velocities.

3.2. Estuarine Structure

3.2.1. Vertical Structure

[28] During flood tides velocity profiles have subsurface maxima that coincide with the elevation of the pycnocline (Figure 4). The elevation of the velocity maxima increases through the tide as the salt wedge advects into estuary and the fresh surface layer thins. The subsurface velocity maximum is characteristic of highly stratified estuaries [*Geyer and Farmer*, 1989] and indicates that bottom boundary layer growth is limited by overlying stratification [*Stacey and Ralston*, 2005]. The model also shows subsurface maxima during floods, although higher in the water column than was observed. Thicker boundary layers during floods in the model indicate too much vertical mixing of momentum. Excess mixing during floods is consistent with other observations that the pycnocline in the model during floods was more diffuse than observed in the field, particularly during high
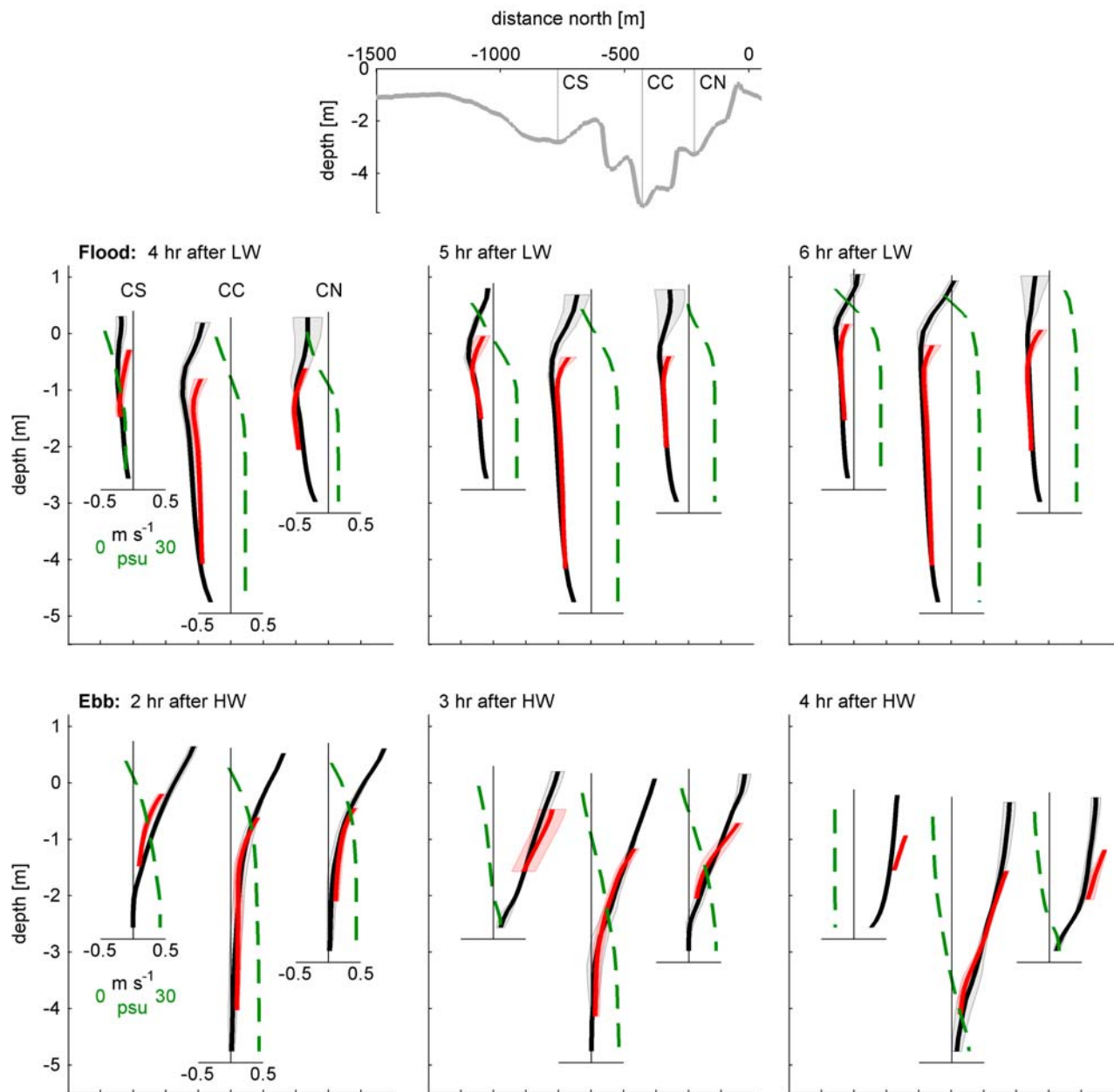
Figure 4. Velocity profiles across the mooring array (central south, central channel, and central north stations). Observed velocities are shown by lighter (red) shading, modeled velocities are shown by dark (black) shading, and modeled salinities are shown by dashed (green) lines. Velocity profiles are phase averaged over 3 days during moderate discharge, with the velocity profile envelope representing variability over the same period. HW, high water; LW, low water.

discharge periods. The discrepancies in stratification were not sensitive to vertical discretization, as 30 σ levels provided results similar to those with 20. The errors likely result from insufficient resolution in both the bathymetric data and the model grid. Excess mixing of momentum and salt may be an effect of insufficient horizontal grid resolution, particularly near the mouth, where high velocities coincide with strong bathymetric gradients (25–35 m grid spacing). Similarly, the relatively large z_0 required to match the observed salt wedge advection would lead to faster growth of the boundary layer and an elevated velocity maximum.

[29] During ebbs the velocity profiles feature strong, nearly linear shear (Figure 4). Early in the ebb, shear is limited to the upper water column and near-bed velocities are negligible. As the ebb progresses, the shear layer moves downward and eventually extends over the entire water column. The base of the shear layer coincides with the base of the pycnocline, and cross-channel gradients in the elevation of the pycnocline depend on the lateral depth variation and lateral circulation (discussed in section 3.2.3). The ebb velocity profiles in the model are consistent with the observations, including the region of zero velocity in the
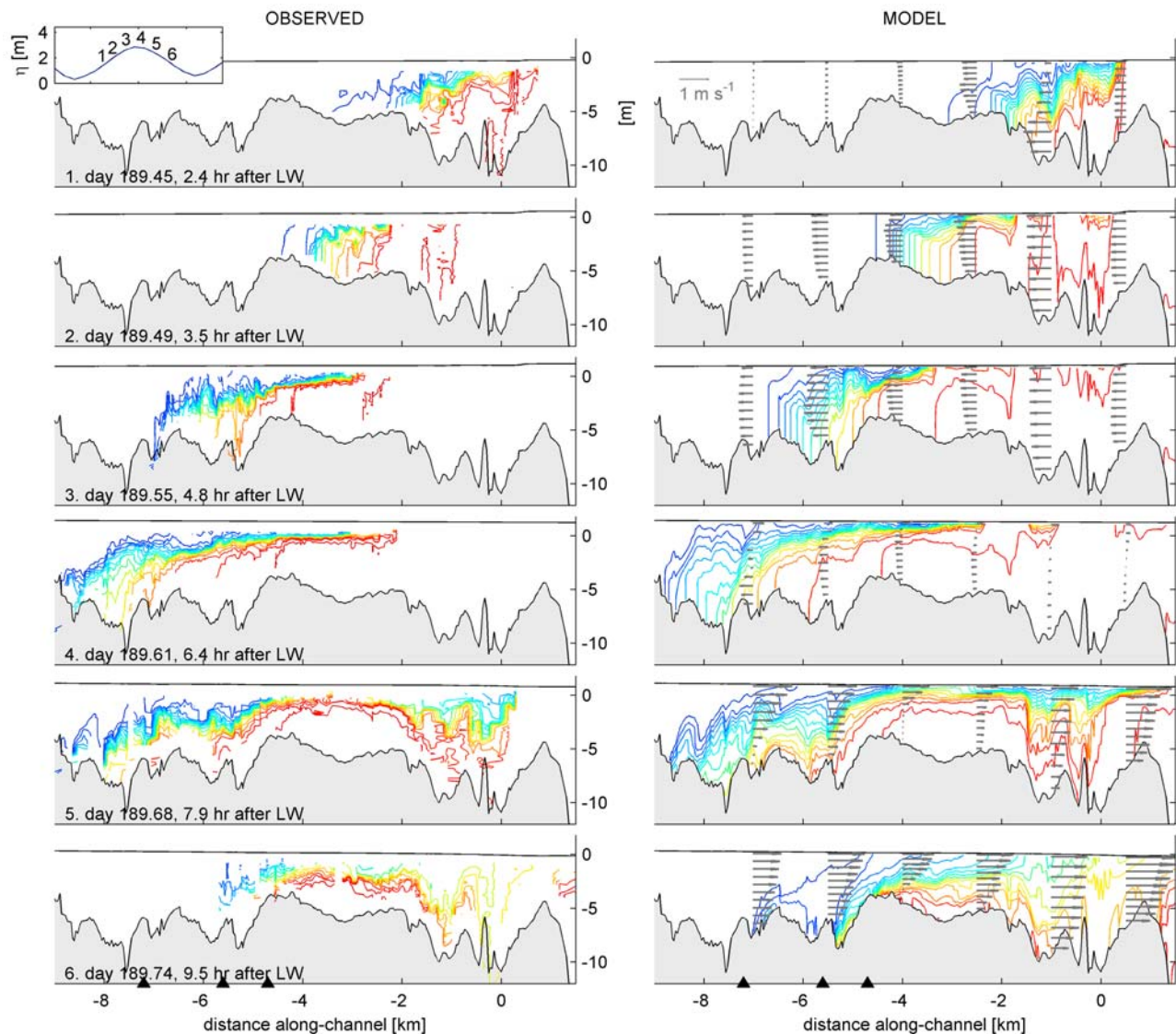
Figure 5. Along-channel salinity distribution: (left) observed and (right) modeled. The year, day, and hour of the transects relative to LW are indicated in each plot, and the tidal stage is shown schematically in the top plot. Salinity contours are every 2 practical salinity units (psu). Transects from the model show the along-channel velocity at several locations along the channel. Arrowheads in bottom plots denote locations of channel constrictions and sills corresponding to bottom fronts.

deeper channel early in the ebb and the magnitude of the shear across the pycnocline.

3.2.2. Longitudinal Structure

[30] The semidiurnal tidal cycle is the dominant frequency of variability in the Merrimack during all but extremely low discharge conditions. Each tidal cycle the salt wedge advances into the estuary during the flood and is largely expelled during the subsequent ebb. We compare observations and model results for the along-channel salinity structure through a tidal cycle with moderate river discharge (280 m^3 s^{-1}) (Figure 5). The model successfully captures the tidal cycle variability in the salinity intrusion, including the along-channel structure of stratification and the development and evolution of bottom and surface salinity fronts.

[31] Beginning shortly after low tide, water from the Gulf of Maine advects into the Merrimack as a bottom front that

formed late in the previous ebb at the bar outside the mouth. In the boundary layer the shear and stratification are weak up to a subsurface velocity maximum, above which the velocity decreases and stratification increases. As the bottom front progresses up-estuary through the flood, a surface tidal intrusion front forms near the mouth. Around high tide the bottom salinity front has extended 8–10 km up-estuary, while the surface tidal intrusion front becomes stationary mid estuary in the region of intertidal flats 3–4 km east of the mouth. Most of the channel from the mid to the upper estuary has strong stratification, with surface-to-bottom salinity differences greater than 25 psu.

[32] After high tide the barotropic pressure gradient reverses and the surface layer begins to ebb. However, the baroclinic pressure gradient due to the bottom front remains strong and near-bottom flow continues up-estuary after the
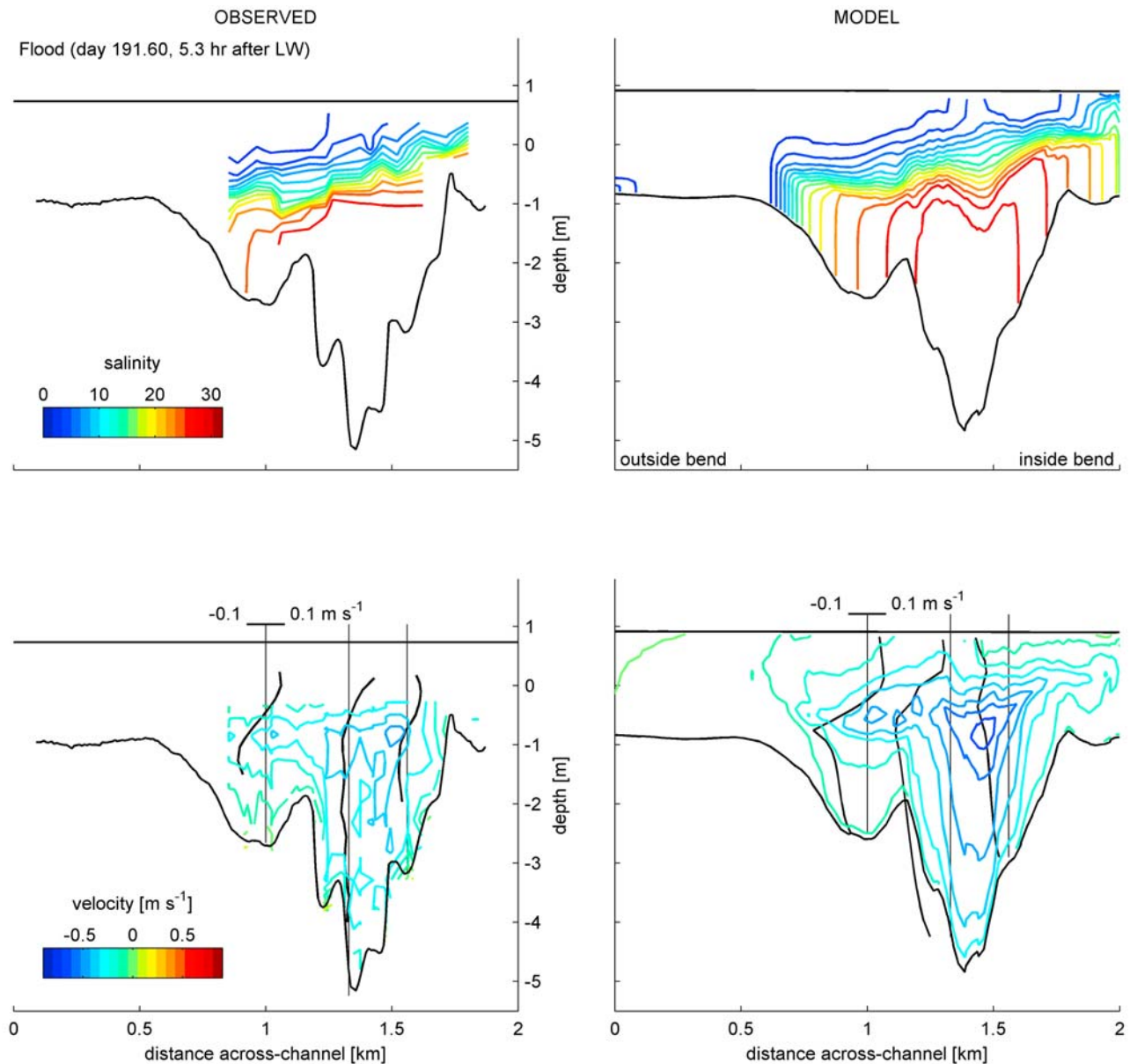
Figure 6. Flood tide cross-estuary transects of (top) salinity and (bottom) velocity, with observations on the left and model results on the right. In the lower plots, cross-channel velocities are charted from the moored observations and from corresponding locations in the model results. Salinity contours are 2 psu, and along-channel velocity contours are 0.1 m s^{-1}.

surface has turned toward ebb. As the ebb progresses the surface flow accelerates and strains the along-channel salinity gradient, increasing the stratification. The baroclinic pressure gradient due to the salinity front opposes the ebb, and near-bottom velocities down-estuary from the front remain near zero. The salinity intrusion retreats through a series of bathymetrically controlled fronts at sills and expansions where the along-channel salinity gradient intensifies (Figure 5). The fronts are associated with strong shear across the pycnocline and shear-induced turbulent mixing. As the salt wedge moves toward the mouth, the fronts break down and stratification is mixed away by bottom-generated turbulence.

3.2.3. Lateral Structure

[33] The focus thus far has been on along-channel variability in salinity and velocity, but the tidal variability in lateral structure is also significant. The lateral distributions of salinity and velocity are shown mid flood (Figure 6) and mid ebb (Figure 7) at a cross section mid estuary (location shown in Figure 2). The cross-channel surveys demonstrate fidelity between the model and the observations not only in local properties observed at moored instruments but also in the three-dimensional structure of salinity and currents.

[34] The lateral velocity and salinity distributions depend on the cross-channel bathymetry and on the channel curvature. During floods the subsurface velocity maximum is apparent across the channel, but velocities are faster in the
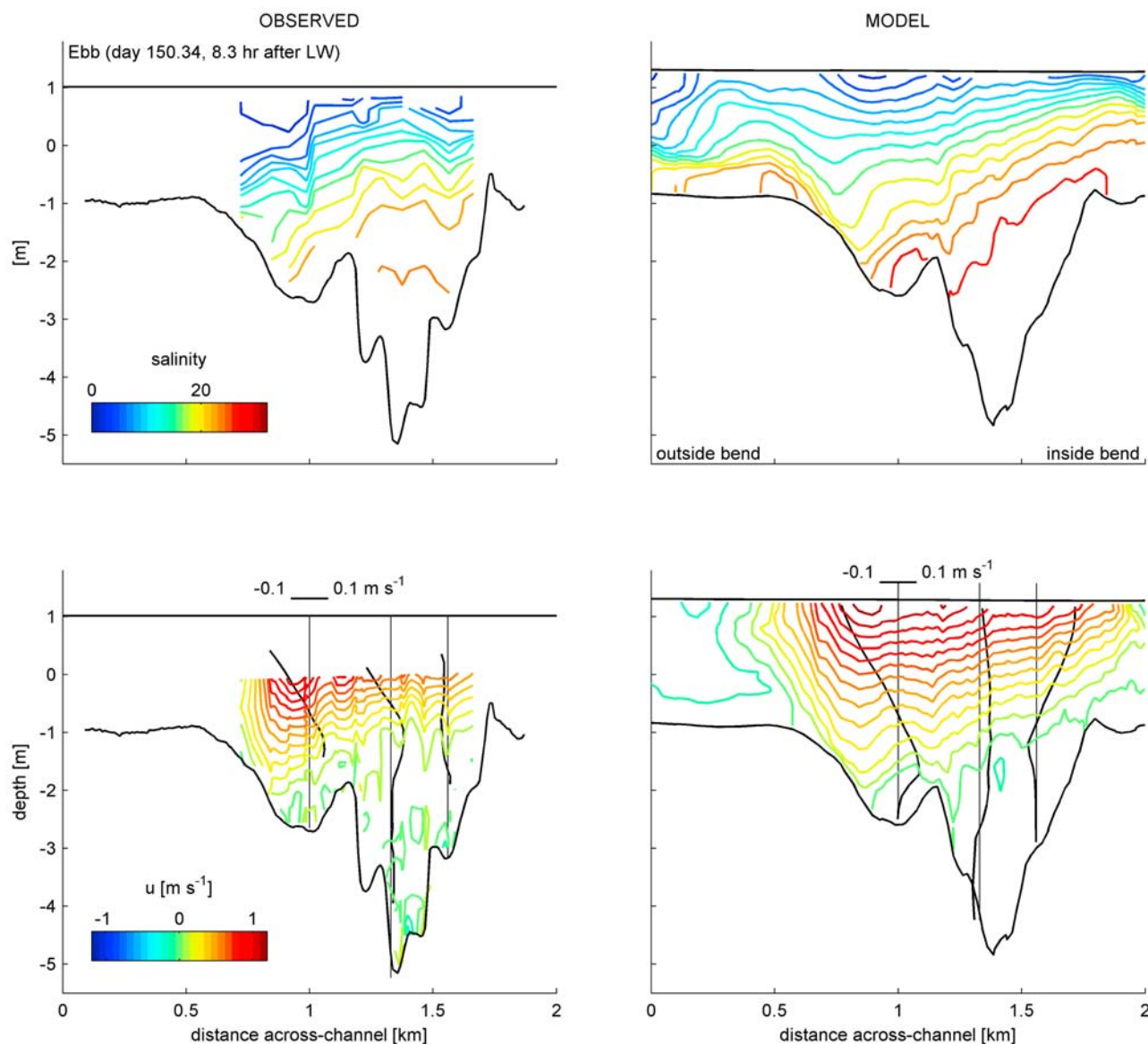
Figure 7. Ebb-tide cross-estuary transects of (top) salinity and (bottom) velocity, with observations on the left and model results on the right, as in Figure 6.

center than on adjacent shoals (Figure 6). The lateral shear in along-channel velocity produces lateral salinity gradients, with saltier water in the channel due to differential advection of the salt wedge [*Nunes and Simpson*, 1985]. The lateral baroclinic pressure gradient generates lateral circulation that transports saltier water onto the shoals. The lateral velocities are divergent from the channel at the elevation of the shoals and convergent at the surface.

[35] The salinity distribution is not symmetric about the channel, as water is fresher on the southern shoals than to the north of the channel. The lateral salinity gradient results from advection of freshwater during the previous ebb. The southern shoals are on the outside of the channel bend. During ebbs, channel curvature forces relatively fresh, high-velocity water near the surface toward the outside (south side) of the bend, with flow toward the inside of the bend at mid depth (Figure 7). This transverse shear creates a lateral salinity gradient as well as lateral shear in along-channel

velocity, with faster ebb velocities and lower salinities on the south side of the channel. The opposing lateral baroclinic pressure gradient might be expected to shut down the curvature-induced lateral circulation [*Seim and Gregg*, 1997; *Chant*, 2002]. Curvature-induced lateral circulation depends on deviations from the depth-averaged velocity [*Kalkwijk and Booij*, 1986; *Geyer*, 1993]. In this location the shear in along-channel velocity across the pycnocline is sufficiently strong to drive curvature-induced lateral circulation against the lateral baroclinic pressure gradient.

[36] The shear across the pycnocline during ebbs results from the strong stratification and from the opposing baroclinic pressure gradient. In the deeper main channel around mid ebb, near-bottom velocities remain near zero and salinities remain high (Figure 5, plots 5 and 6, and Figure 7). The baroclinic pressure gradient due to the along-channel slope of the halocline increases with depth and opposes the ebbing tidal barotropic pressure gradient. The strong lon-
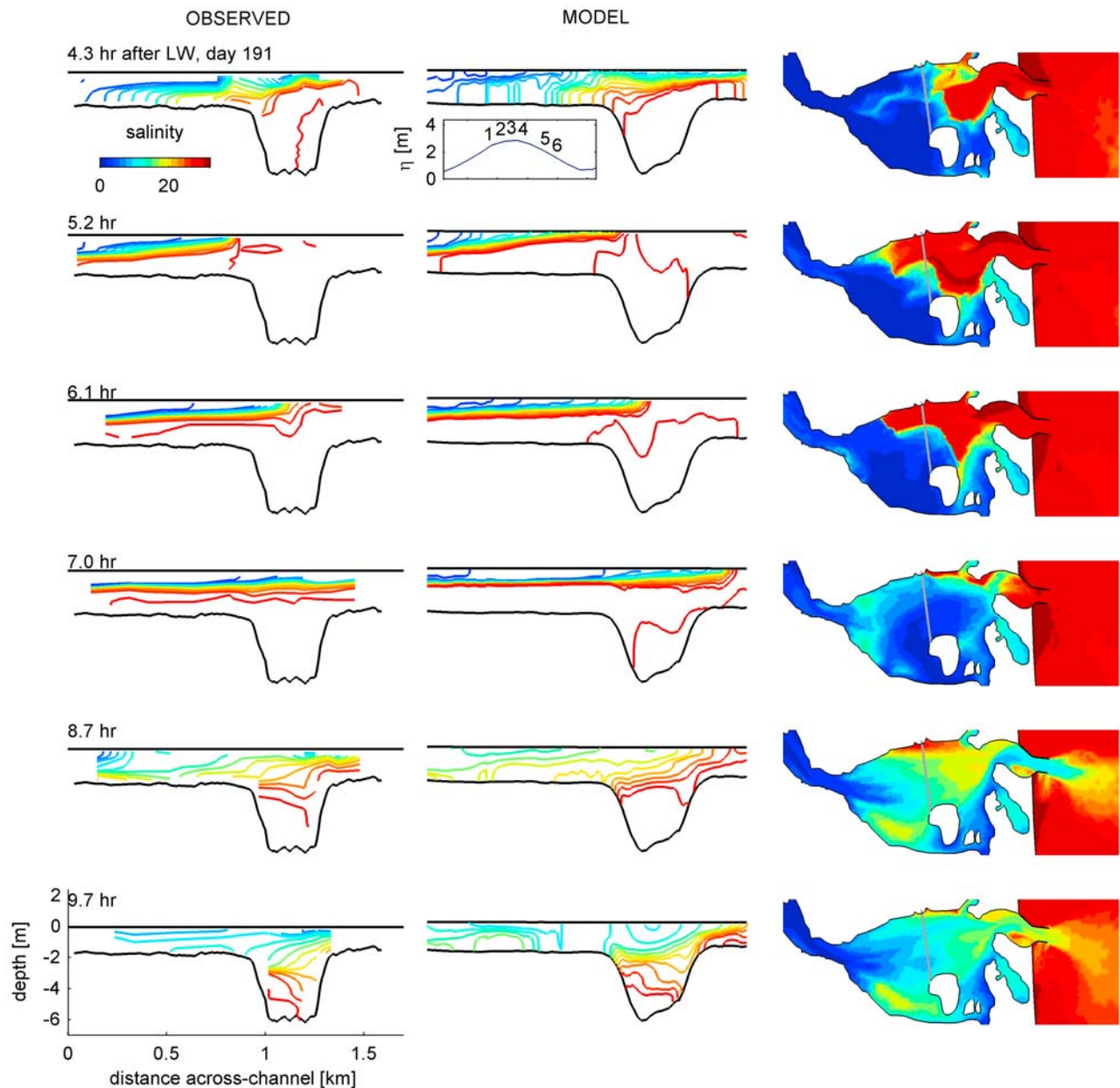
Figure 8. Tidal intrusion front development and dissipation in (left) the observations and (center and right) the model results. Salinity contours are 2 psu, and plan maps of surface salinity are on the right. The time of each transect relative to LW is printed in each plot and shown schematically in the top plot.

gitudinal salinity gradient combines with the bathymetry to produce tidal asymmetry in the lateral distribution of flow. The deeper channel to the north is flood dominant, with stronger velocities during the flood tide than the shoals or the shallower channel to the south. During ebbs, flow remains near zero in the deeper channel and low-salinity water moves seaward predominantly via the shallower, ebb-dominant southern channel. Similar lateral segregation of the flow into adjacent flood- and ebb-dominant channels has been observed in the Columbia River [*Jay and Smith*, 1990b]. The asymmetry in the lateral distribution of velocity and salinity creates a lateral structure in the tidally averaged salt flux [*Fischer*, 1972], but as shown in the next

section, the lateral steady flux remains small relative to the tidal salt flux.

[37] The heterogeneous bathymetry and strong salinity gradients create a complex, three-dimensional flow. Only by resolving the bathymetry and salinity gradients can the model reproduce important features of the flow. For example, during periods of moderate to high discharge, a tidal intrusion front moves upstream through the mouth region around each high tide (Figure 8). As the front advances into the broad flats mid estuary it becomes strongly asymmetric owing to bathymetry and the lateral gradient in outflow [*Largier*, 1992]. The surface front advances farther upstream on the northern side of the estuary. Channel curvature creates cross-channel shear and sets up a lateral baroclinic

gradient, with lower salinities and stronger down-estuary velocities on the southern shoal that oppose the advance of the front. Flow is convergent toward the front, with accumulation of buoyant material and organisms that can be biologically important for larval transport and the concentration of prey [*Franks*, 1992; *Eggleston et al.*, 1998; *Mendes et al.*, 2002]. After high tide the intrusion front begins to retreat down-estuary, and by mid ebb it has dispersed.

4. Analysis

4.1. Salt Flux

[38] Using both observations and simulations of the salinity and velocity fields, we examine the exchange of salt between the estuary and the coastal ocean. To assess the salt flux mechanisms the salinity and velocity fields over a tidal cycle are decomposed both spatially and temporally into mean components and deviations from the means. In this analysis we follow the approach described by *Lerczak et al.* [2006] but note that other approaches produce slightly different flux distributions, depending on the sequence of spatial and temporal averaging.

[39] At four cross sections (locations in Figure 2), we analyzed data from multiple M_2 tidal cycle surveys of salinity and velocity spanning discharge between 200 and 550 m^3 s^{-1} (three to five tidal cycles at each cross section). The salinity and velocity observations were gridded onto regular spatial grids using σ coordinates and interpolated onto uniform time series with 30 increments over 12.42 h. Near-bottom and near-surface gaps in the ADCP velocity were filled by vertical extrapolation assuming zero velocity at the bottom and zero shear at the surface. The tidal cycle surveys spanned the navigable extent of each cross section, but parts of the broad flats mid estuary were too shallow for the survey vessel around low tide. At those times salinities and velocities were extrapolated laterally by assuming that salinity was laterally uniform and that depth-averaged velocities decreased inversely with water depth. The lateral extrapolation does not account for the strong gradients at shear fronts that were observed at the transition onto the intertidal shoals. However, flows on the shoals at these times were relatively shallow and weak, and they did not contribute significantly to the total salt flux. Lateral extrapolation using alternative methods did not change the results significantly.

[40] As a check on the completeness of the tidal cycle transects, we calculated the freshwater volume flux at each cross section. The freshwater fraction is the normalized difference between the oceanic (s_{oc}) and the measured salinities. The freshwater flux is integrated across each cross section through the tidal cycle:

$$Q_f = \frac{1}{T} \int_{tide} \left[\int_{area} \frac{s_{oc} - s}{s_{oc}} u dA \right] dt. \tag{5}$$

The freshwater fluxes calculated from the tidal cycle surveys corresponded with the river discharge at the gage upstream to within about 10%. This provides some confidence that the spatial and temporal coverage of the surveys was sufficient to resolve the salt flux.

[41] To quantify the salt flux the gridded velocity and salinity fields were decomposed into three orthogonal components: tidally and cross-sectionally averaged (u_o and s_o), tidally averaged and cross-sectionally varying (u_e and s_e), and tidally and cross-sectionally varying (u_t and s_t) values [*Lerczak et al.*, 2006]. Taking velocity, for example, the decomposition becomes

$$
\begin{aligned}
u_o &= \frac{1}{A_o} \left\langle \int (u(y,z,t)) dA \right\rangle, \\
u_e(y,z) &= \left\langle \frac{A}{A_o} u(y,z,t) \right\rangle - u_o, \\
u_t(y,z,t) &= u(y,z,t) - u_o - u_e(y,z),
\end{aligned} \tag{6}
$$

where angle braces indicate tidal averages, the area integration limits are vertically from 0 to 1 σ and laterally from 0 to the cross-sectional width, and A_o is the tidally averaged cross-sectional area. The component u_o is uniform over the cross section and varies at subtidal time scales, the component u_e has a spatial structure and varies at subtidal time scales, and the component u_t varies spatially and tidally. The decomposition of salinity is analogous, and the total salt flux (F_s) is the product of the components:

$$F_s = \left\langle \int (u_o s_o + u_e s_e + u_t s_t) dA \right\rangle = -Q_r s_o + F_e + F_t, \tag{7}$$

where $Q_r s_o$ is advection of salt out of the estuary by the river, F_e is the salt flux into the estuary by steady shear dispersion, and F_t is the tidal oscillatory salt flux.

[42] In many partially mixed estuaries, steady vertical shear and stratification due to the along-estuary salinity gradient dominate the salt flux [e.g., *Lerczak et al.*, 2006]. Alternatively, lateral shear and salinity gradients arising from cross-channel bathymetry can generate steady, laterally varying exchange [*Fischer*, 1972]. In this decomposition we do not distinguish between vertical and lateral structure of the steady salt flux but, rather, integrate over the entire cross section. The Merrimack has strong vertical and cross-channel gradients in salinity and velocity such that the vertical and lateral components of the steady flux are both important and difficult to separate.

[43] The tidal oscillatory salt flux depends on correlations between salinity and velocity at tidal time scales. Various mechanisms can shift salinity and velocity out of quadrature to produce tidal fluxes, including tidal pumping at a constriction [*Stommel and Farmer*, 1952], trapping in side embayments [*Okubo*, 1973], and lateral stirring [*Banas et al.*, 2004]. Tidal fluxes are often important in estuaries with heterogeneous bathymetry, particularly where the spacing between topographic features is less than a tidal excursion [*Geyer and Signell*, 1992].

[44] The relative contribution of the steady and tidal components can be written as the ratio $\nu = F_t/(F_e + F_t)$ [*Hansen and Rattray*, 1966], where tidal oscillatory fluxes dominate the total up-estuary salt flux for ν approaching 1. We calculated ν based on the tidal cycle surveys at the four cross sections (Figure 9). The range of values at each cross section depends on variability in forcing within the observations but also reflects uncertainty in the survey calculations. A comparison of the freshwater flux with the gaged
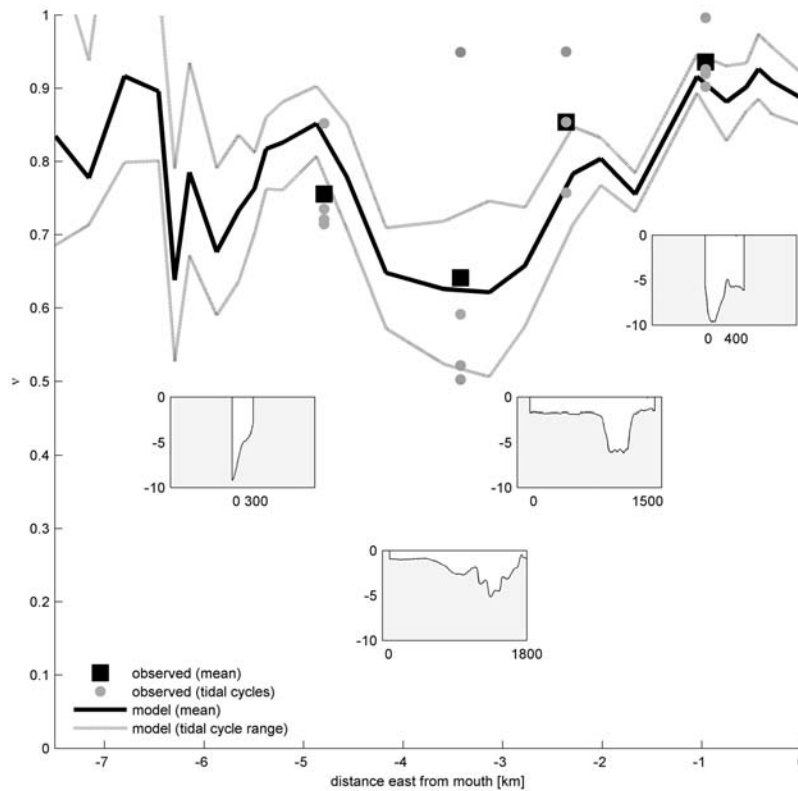
Figure 9. Fraction of the total up-estuary salt flux due to tidal processes (ν = (tidal salt flux)/(tidal + steady salt flux)) versus distance from the mouth. Observations at four cross sections are shown by symbols: circles for each tidal cycle survey and squares for the cross-section mean. Tidal cycle surveys were made on 17, 18, and 30 May and 7 and 10 July 2005 (not all cross sections were surveyed every day), and cross-sectional bathymetries are shown in insets below the curves. From model results, the average ν was taken at regularly spaced cross sections along the estuary (solid line), and dotted lines show the variability in ν from tidal cycles extracted over the observation period.

discharge upstream indicated errors of around 10%, but the ratio of the salt flux components may be more sensitive to incomplete spatial and temporal resolution in the cross-sectional data.

[45] For comparison we have taken model simulations corresponding to the observations and followed a similar decomposition of the salinity and velocity fields. Cross sections are extracted at regular intervals along the main channel (approximately every 400 m), and the steady shear and tidal oscillatory salt fluxes are calculated for several tidal cycles. The resulting ν values compare well with the observations (Figure 9). In the model results the range of ν values at each location is due to variability in tidal and fluvial forcing during the period of simulation.

[46] Tidal processes dominate relative to the steady salt flux in the Merrimack, with ν ranging between 0.5 and 0.9. The strong along-estuary salinity gradient might be expected to drive baroclinic exchange and steady salt flux, but the tidal variability in salinity and velocity due to advection of the salt wedge is far greater than the tidally averaged circulation. The steady flux is maximal mid estuary (2 to 4 km from the mouth), where the steady exchange has both vertical and lateral structure. The vertical structure is due to the stratification and baroclinic circulation, while the lateral structure results from the channel curvature and

cross-channel bathymetry as discussed in section 3.2.3. However, steady fluxes account for less than half of the total up-estuary salt flux in all of the discharge and tidal conditions examined.

[47] The mechanisms of tidal oscillatory flux are difficult to distinguish. Near the constriction at the mouth, tidal pumping appears to dominate as saltier water advects in during flood and fresher water flows out at peak ebb [*Stommel and Farmer*, 1952]. Inside the estuary the tidal salt flux is consistent with tidal asymmetry in the elevation of the halocline and the vertical structure of the tidal currents [*Jay and Smith*, 1990a; *Kay et al.*, 1996]. During floods the halocline is high in the water column and the velocity profile below it is relatively uniform. During ebbs the halocline is lower in the water column and more diffuse, and the velocity profile is more sheared. Consequently transport mid water column during ebbs is fresher than during floods, and net salt flux is up-estuary. Similar processes have been observed in the Hudson River estuary during high discharge, where the halocline oscillated tidally in hydraulic response to a constriction [*Geyer and Nepf*, 1996]. An analytical model of a shallow, highly stratified estuary representative of the Columbia River estuary showed up-estuary salt flux due to tidal correlations in elevation and thickness of the halocline [*Jay and Smith*, 1990a]. The pattern of a relatively
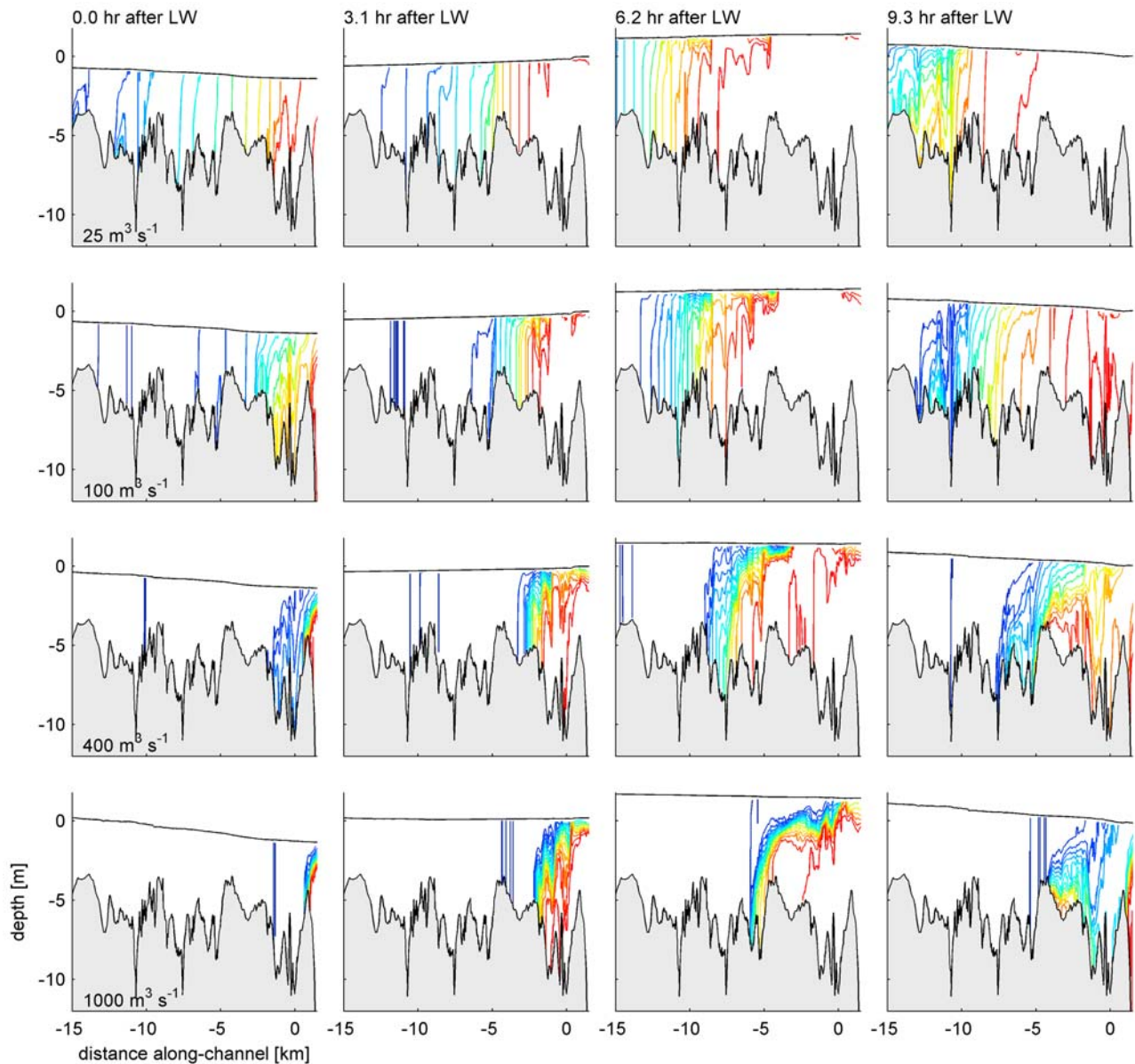
Figure 10. Along-channel salinity distributions from the model over a range of river discharges ((top row) 25 m^3 s^{-1} and (bottom three rows) 100, 400, and 1000 m^3 s^{-1}), with a constant tidal range of 2.8 m. Snapshots are shown through the tide (leftmost column) at LW and (right three columns) at mid flood, HW, and mid ebb.

thin halocline high in the water column during floods and a thicker halocline with stronger shear during ebbs occurs in the Merrimack over a broad range of discharge and tidal amplitudes, and it appears to be a primary mechanism for tidal salt flux. However, the bathymetric complexity of the Merrimack makes it difficult to distinguish distinct salt flux mechanisms, and more complete characterization of this tidal asymmetry in shear and stratification remains for future research.

4.2. Estuarine Parameter Dependence

[48] In addition to the observation period, we modeled a range of idealized conditions with M$_2$ tidal forcing (2.0, 2.4, 2.8, and 3.2 m range) and constant river discharge (25, 50, 100, 200, 400, 700, 1000, and 2000 m^3 s^{-1}). The tidal ranges reflect spring-neap variability, and discharges span from low flow to approximately the 20 year flow event. In each case forcing was held constant until the system reached a tidal equilibrium, which was typically within 4 tidal cycles for moderate and high discharge cases but up to 10 tidal cycles for lower discharges.

[49] Over the range of parameter space tested, conditions in the Merrimack depend primarily on river discharge and are relatively insensitive to tidal amplitude. This differs from partially stratified estuaries like the Hudson, where spring-neap shifts in tidal mixing significantly alter the salinity intrusion length and stratification [e.g., *Lerczak et al.*, 2006]. At higher discharge the Merrimack is short and strongly
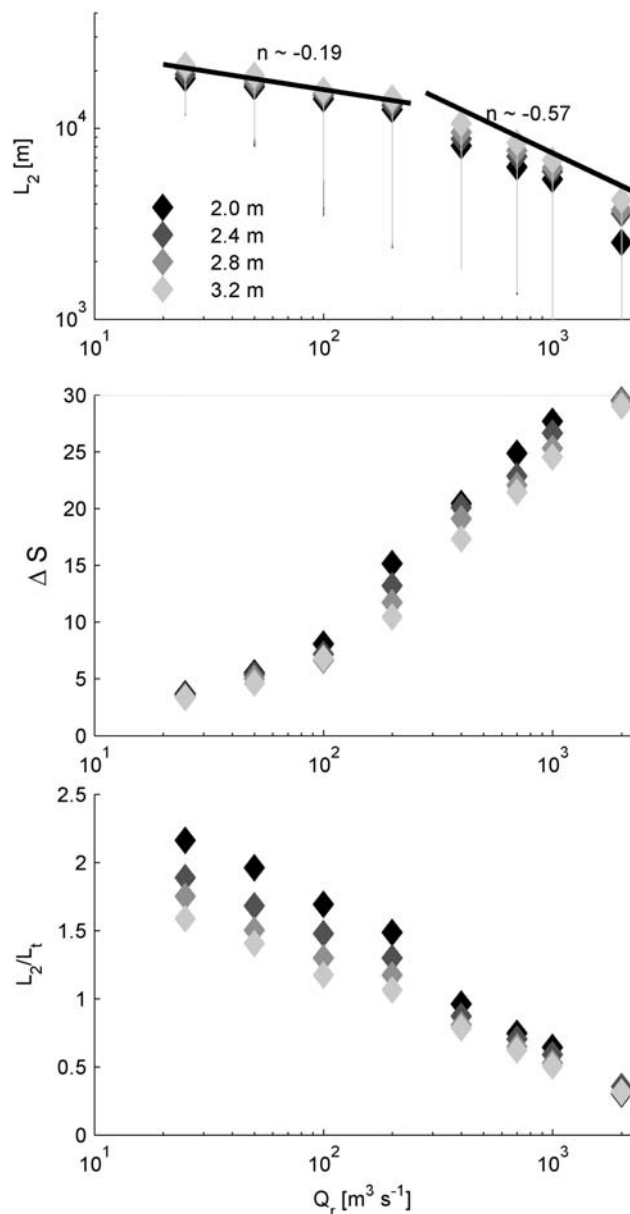
Figure 11. Discharge dependence of salinity intrusion and stratification. (top) Salinity intrusion (2 psu) versus river discharge for a range of tidal amplitudes. Diamonds show maximum extent of salinity intrusion, while vertical lines show a range of 2 psu isohaline through the tide. Best-fit slopes are shown for lower discharge ($L_2 \sim Q_r^{-0.19}$ for $Q_r < 300$ m^3/s) and for higher discharge ($L_2 \sim Q_r^{-0.57}$ for $Q_r > 300$ m^3/s) conditions. (middle) Stratification (tidal average of the surface-to-bottom salinity difference at the 15 psu isohaline) as a function of river discharge. (bottom) Salinity intrusion length normalized by tidal excursion length (L_t) as a function of river discharge.

stratified, while at lower discharge the system becomes longer and more weakly stratified. Four discharges with the same tidal amplitude (2.8 m range) are shown at low water, mid flood, high water, and mid ebb (Figure 10). In the lower discharge cases mid-salinity mixed water is retained in the estuary at low tide, the horizontal density gradient is com-

paratively weak, and the maximum stratification occurs during the ebb. In the higher discharge cases the estuary is almost entirely fresh at low tide and a bottom salinity front forms at the mouth bar. Stratification during high discharge is greatest at the end of the flood and significant mixing occurs during the ebb.

4.2.1. Salinity Intrusion Length

[50] The length of the estuary (L_x), or the maximum tidal extent of the 2 psu isohaline, depends largely on discharge rather than tidal amplitude (Figure 11). At low discharge ($Q_r < 300$ m^3 s^{-1}) $L_2 \sim Q_r^{-0.19}$, while at higher discharges $L_2 \sim Q_r^{-0.57}$. For comparison, a scaling of the steady salt balance where baroclinic exchange dominates the up-estuary salt flux yields $L_x \sim Q_r^{-1/3}$ [*Monismith et al.*, 2002]. For most tidal processes the up-estuary salt flux is assumed to depend on U_t and not on Q_r [*Geyer and Signell*, 1992]. Scaling for the salinity intrusion where tidal salt fluxes dominate is more sensitive to discharge than the baroclinic exchange case, with $L_x \sim Q_r^{-1}$ [*MacCready*, 2007; *Lerczak et al.*, 2009].

[51] Neither the $Q_r^{-1/3}$ nor the Q_r^{-1} scaling corresponds to the observed discharge dependence in the Merrimack. Several incorrect assumptions could contribute to the discrepancy. We assumed that the tidal dispersion depended only on U_t and was independent of Q_r. However, the primary mechanism of tidal salt flux observed in the Merrimack depends on asymmetry in the elevation and thickness of the halocline. River discharge can affect both the initial thickness of the halocline during flood tides (sharper for high Q_r) and the shear and mixing across the interface during ebbs (more shear for high Q_r).

[52] The scaling also assumed uniform along-channel bathymetry. In reality, bathymetry varies along the estuary, and the effective depth and cross-sectional area depend on the position of the salinity intrusion. Including variations in cross-sectional area, we found (using least-squares curve fitting) that the length of the salinity intrusion could be scaled by the tidal (U_t) and river ($U_r = Q_r/A_x$) velocities:

$$L_x \sim U_t^{0.36}(Q_r/A_x)^{-0.33}, \qquad (8)$$

where A_x is the average cross-sectional area in the estuary where salinity is >2 psu. Note that this scaling is empirical and is not well constrained, owing to the limited data and bathymetric irregularities, but it is instructive for comparing the Merrimack to scaling for other estuaries. The length of the salinity intrusion increases moderately with tidal amplitude and has an inverse dependence on discharge. Compared with Q_r^{-1} for tidal fluxes that are independent of discharge, the weaker dependence implies that up-estuary tidal flux increases with Q_r. Higher river discharge can enhance the tidal salt flux in the Merrimack by increasing the tidal asymmetry in the elevation and thickness of the halocline, making the estuary less sensitive to changes in discharge than the Q_r^{-1} expected for other tidal salt flux mechanisms.

[53] Increases in tidal amplitude also enhance the up-estuary salt flux, but the dependence is weaker than for other tidal processes. The up-estuary fluxes due to tidal pumping [*Stommel and Farmer*, 1952], lateral trapping [*Okubo*, 1973], and tidal random walk [*Zimmerman*, 1986] result in scaling for the salinity intrusion as $L_x \sim U_t^2$, while oscillatory shear dispersion [*Fischer et al.*, 1979] and lateral
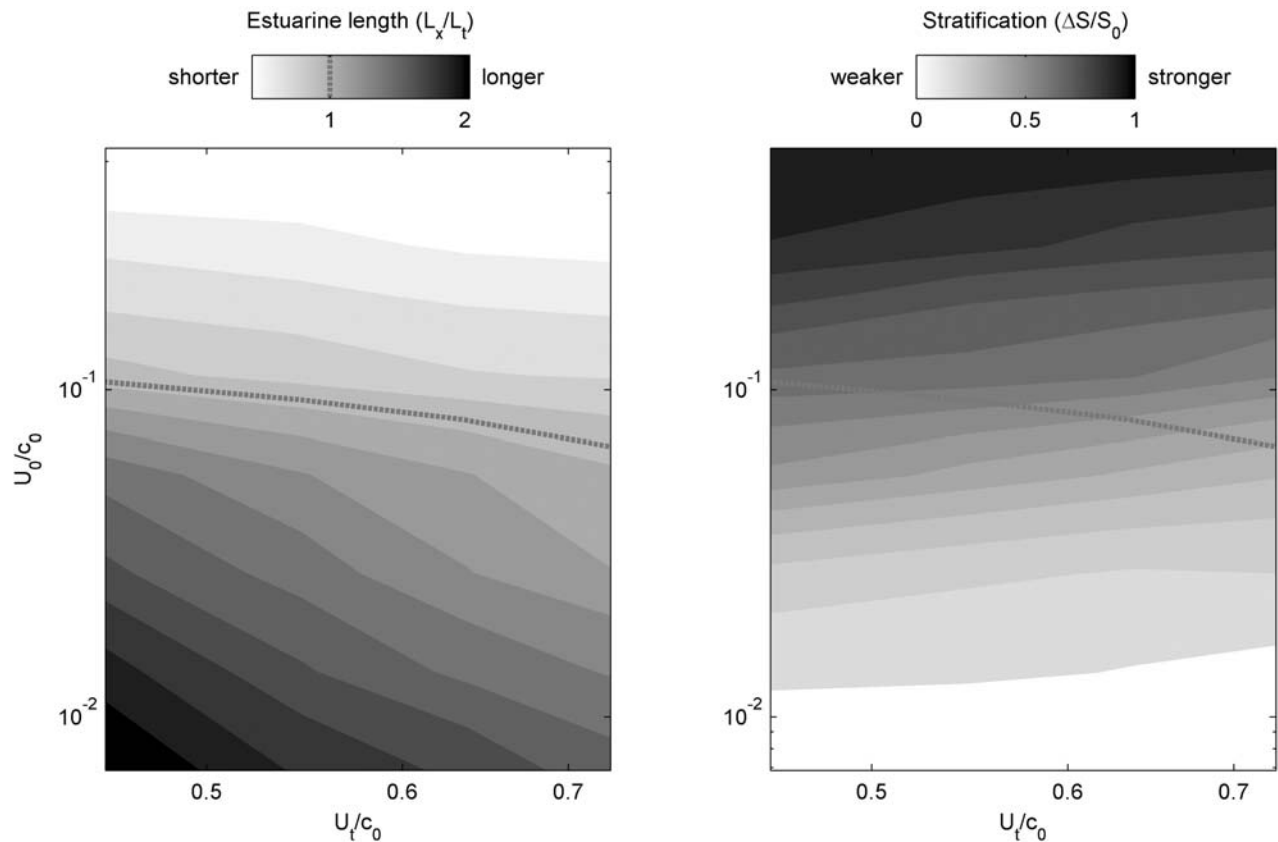
Figure 12. Normalized salinity intrusion and stratification in estuarine parameter space. Salinity intrusion (L_x, 2 psu isohaline) is normalized by tidal excursion (L_t), and stratification (surface-to-bottom salinity difference at the 15 psu isohaline) is normalized by oceanic salinity (s_o). Each is contoured as functions of a tidal Froude number (U_t/c_0) and a freshwater Froude number (U_0/c_0). The dashed line in both plots is the contour of $L_x/L_t = 1$.

stirring [*Banas et al.*, 2004] scale linearly with tidal velocity, or $L_x \sim U_t$. In contrast, the steady baroclinic salt flux depends inversely on tidal velocity: as tidal mixing increases, estuarine circulation and stratification weaken and the steady exchange decreases, with the net effect that $L_x \sim U_t^{-1}$. In the Merrimack, increases in tidal amplitude tend to increase the shear and thickness of the pycnocline during ebbs. However, increased tidal amplitude also increases mixing and reduces stratification during floods, decreasing the tidal asymmetry in stratification. The combination of the weak influence of tidal amplitude on the tidal salt flux and the inverse dependence of the steady flux makes the length salinity intrusion relatively insensitive to tidal amplitude. While the scaling with discharge of $Q_r^{-0.33}$ is similar to that found in other estuaries, the tidal velocity scaling of $U_t^{0.36}$ is weaker than the theoretical predictions of U_t^{-1} for baroclinic exchange or U_t^2 to U_t^1 for tidal salt flux. Consequently, over the observed conditions the length of the estuary varied more in response to river discharge than to spring-neap shifts tidal range.

4.2.2. Stratification

[54] At high discharge the Merrimack is strongly stratified, while at low discharge the stratification becomes weaker (Figure 11). Stratification is measured in a discharge- and tide-dependent location (where the depth-averaged salinity is 15 psu) rather than at a fixed location because the position

of the salinity intrusion varies with forcing. At the highest discharges the tidally averaged surface-to-bottom salinity difference approaches the oceanic salinity (30 psu in these cases), and for much of the tidal cycle nearly fresh water exits the estuary. In moderate to high discharge cases, the maximum N^2 occurs during flood tides, as a thin halocline near the surface overlies a thicker bottom layer of uniform, oceanic salinity. During ebbs the halocline mixes and broadens, and N^2 decreases (Figure 10). For lower discharge cases stratification is weaker. During floods the salinity field is nearly uniform vertically, with the exception of thin surface layers of stratification at topographically controlled bottom fronts that formed during the previous ebb. Maximum stratification for low discharge conditions occurs during ebbs as the shear in the along-channel velocity strains isohalines [*Simpson et al.*, 1990].

[55] The transition from strong stratification with the tidal maximum during floods to more weakly stratified conditions with the maximum stratification during ebbs occurs around the discharge at which the length of the salinity intrusion is approximately equal to the length of the tidal excursion, $L_t = (U_t T_t)/\pi$ (Figure 11). Strong stratification during floods is generated only when the bulk of the salinity intrusion is expelled at the end of each ebb tide. For these discharge conditions, nearly fresh water flows over the bar and the mouth at the end of the ebb, detaching from the

Table 2. Characteristics of Estuaries with Forcing Parameters Similar to the Merrimack Taken from the Literature[a]

Estuary	H (m)	Q_r ($\text{m}^3 \text{ s}^{-1}$)	U_0 (m s^{-1})	U_t (m s^{-1})	L_t (km)	L_x (km)	Δs (psu)	U_0/c_0	U_t/c_0	Source
Columbia	15	16000	0.3	1.4	20	25	25	0.2	0.7	*Jay and Smith* [1990b]
Fraser	10	3000	0.3–0.4	1.0	20	20–35	25	0.2–0.3	0.6–0.7	*Geyer and Farmer* [1989]
Connecticut	8	560	0.3–0.4	0.6	6	5–20	15	0.2–0.3	0.4	*Garvine* [1975]
Snohomish	4	300	0.25	0.5–0.8	15	15	20	0.3	0.6–0.9	*Wang et al.* [2009]
Merrimack	5	220	0.15–0.4	0.6–0.9	8–12	6–10	20–25	0.1–0.3	0.5–0.7	This study
Tweed	3	140	0.15	0.3–0.4	5	5	20	0.2	0.4–0.5	*Uncles and Stephens* [1996]
Tidal creek, San Francisco Bay	1	0.4	0.1–0.2	0.3			15	0.2–0.3	0.6	*Ralston and Stacey* [2007]

[a]Cases listed have moderate to high discharge (equal to or greater than the annual mean), and scales for depth, discharge, velocities, tidal excursion, salinity intrusion length, and stratification are representative.

bottom and spreading radially as a surface plume. A bottom salinity front forms at the crest of the bar below the plume liftoff (e.g., $Q_r = 400$ or 1000 $\text{m}^3 \text{ s}^{-1}$ in Figure 10). During the flood tide the two-layer structure advects strong stratification into the estuary. Bottom stress is relatively low and constant during the flood, and the maximum bottom stress occurs mid to late ebb and coincides with the breakdown of stratification.

[56] When the discharge is low ($Q_r < {\sim}200$ $\text{m}^3 \text{ s}^{-1}$) and the salinity intrusion is greater than a tidal excursion, a front does not form at the mouth and flood tides are nearly well mixed. Stratification develops during ebbs owing to tidal straining, but the longitudinal salinity gradients and the ebb shears are weaker during low discharge conditions than for more frontal conditions during high discharge. Even under low discharge conditions, sills and expansions create heterogeneity in the stratification through the formation of local bottom fronts. Maximum bottom stresses during low discharge conditions occur during floods, with lower bottom stresses during ebbs associated with the increased stratification. Generally, the shift from an estuary where strong stratification is created at the downstream boundary and is maximal during flood tides to a more moderately stratified system where stratification is created during ebb tides by tidal straining depends on discharge and occurs when the length of the salinity intrusion is similar to the tidal excursion.

4.2.3. Dimensionless Forcing Scales

[57] Rather than absolute magnitudes of discharge and tidal amplitude, the estuarine response depends on the relative balance among fluvial, tidal, and baroclinic forcing. To facilitate comparison of these results with other systems, we consider the salinity intrusion and stratification in terms of dimensionless ratios of velocity scales [*MacCready*, 1999]. The advective velocity is $U_0 = Q_r/A$, where A is the cross-sectional area, equal to the depth H times the width B. The tidal velocity is $U_t = \frac{1}{2}(\eta/H)(gH)^{1/2}$, where η is the tidal amplitude. (The factor of $\frac{1}{2}$ makes U_t correspond roughly with observed tidal velocities.) The baroclinic velocity is $c_0 = (g\beta s_{oc}H)^{1/2}$, where β is the coefficient of expansivity for salinity (7.7×10^{-4} psu^{-1}) and s_{oc} is the oceanic salinity. Using constant values for H and B of 7 and 400 m, respectively, these velocity scales depend only on the external forcing and are independent of estuarine response.

[58] We normalize the salinity intrusion by the tidal excursion (L_x/L_t), and the stratification by oceanic salinity ($\Delta s/s_o$) (Figure 12), and contour each as a function of a tidal Froude number (U_t/c_0) and a freshwater Froude number ($U_0/$

c_0). The transition between a short ($L_x/L_t \approx 1$), strongly stratified ($\Delta s/s_{oc} > 0.5$) estuary and a longer, more moderately stratified estuary occurs around $U_0/c_0 \approx 0.1$. Similarly, stratification in the estuary depends predominantly on the discharge rather than tidal amplitude over the range tested. Around the transition of $U_0/c_0 \approx 0.1$, the normalized stratification is about 0.5, with weaker stratification for lower discharges.

5. Discussion

[59] Conditions in the Merrimack are representative of similar estuaries where relatively large river and tidal velocities coincide with shallow bathymetry. Examples span orders of magnitude of mean annual discharge, including the Columbia ($Q_{\text{mean}} = 7500$ $\text{m}^3 \text{ s}^{-1}$) [*Jay and Smith*, 1990b], Fraser ($Q_{\text{mean}} = 3600$ $\text{m}^3 \text{ s}^{-1}$) [*Geyer and Farmer*, 1989], Connecticut ($Q_{\text{mean}} = 520$ $\text{m}^3 \text{ s}^{-1}$) [*Garvine*, 1975], Snohomish ($Q_{\text{mean}} = 270$ $\text{m}^3 \text{ s}^{-1}$) [*Wang et al.*, 2009], and Tweed ($Q_{\text{mean}} = 80$ $\text{m}^3 \text{ s}^{-1}$) [*Uncles and Stephens*, 1996] estuaries. Similar conditions have also been observed in shallow distributary channels through tidal flats in San Francisco Bay, where $Q_{\text{mean}} < 1$ $\text{m}^3 \text{ s}^{-1}$ [*Ralston and Stacey*, 2007]. To illustrate the common parameter space, we have taken velocity and depth scales for these estuaries from the literature (Table 2). We emphasize that these estimates are crude and note that we have focused on periods with relatively high discharge (equal to or greater than the annual mean) and strong stratification. During moderate to high discharge, all of these systems occupy a similar part of parameter space, with $U_0/c_0 \approx 0.2$ to 0.3 and $U_t/c_0 \approx 0.5$ to 0.8. These estuaries are short relative to their tidal excursion, with L_x/L_t between 1 and 2, and are strongly stratified, with surface-to-bottom differences of 15 to 25 psu.

[60] Several important attributes distinguish the Merrimack and similar strongly forced estuaries from deeper systems with weaker tidal and river forcing. In the Merrimack strong stratification develops when the salinity intrusion is less than or equal to the tidal excursion so that a bottom salinity front is formed prior to each flood tide. Because of the shallow flows and strong tidal velocities, vertical mixing is rapid relative to the tidal cycle. Strong river velocities and stratification confine the mixing to maximum ebb during high discharge conditions, and thus the flood and early ebb are strongly stratified. During low discharge conditions ($Q_r < 100$ in the Merrimack), the salinity intrusion expands upstream and the estuary is more weakly stratified. Tides continue to mix during ebbs, but a

strong salinity gradient and halocline are not regenerated for each flood. Stratification created at a mouth bar during high discharge (and low-discharge neap tides) was also identified as an important boundary condition for the Columbia River estuary [*Jay and Smith*, 1990a].

[61] The dominance of tidal salt fluxes over residual circulation appears to be common to shallow, strongly stratified estuaries. In the Columbia River reported values of ν ranged from 0.59 during a low discharge period to 0.67 during high discharge [*Hughes and Rattray*, 1980]; another study with low discharge found ν to be 0.63 [*Kay et al.*, 1996]. The predominance of oscillatory tidal salt flux distinguishes the Merrimack and similar estuaries from partially mixed estuaries where steady shear flow accounts for most of the up-estuary salt flux. For example, in the Hudson River estuary residual circulation dominates the up-estuary salt flux and ν ranges from 0 to 0.3 during moderate to high discharge periods [*Hunkins*, 1981; *Lerczak et al.*, 2006]. Tidal pumping can be important during lower discharge periods and spring tides ($\nu = 0.3$ to 0.8) [*Bowen and Geyer*, 2003; *Lerczak et al.*, 2006] and at bathymetric features like constrictions [*Kay et al.*, 1996].

[62] Another conceptual distinction between short, stratified estuaries and longer partially mixed systems is the dominant time scale of variability. Estuarine response time scales as the length of the estuary divided by the freshwater velocity (L_x/U_0) [*Kranenburg*, 1986], so short, river-dominated estuaries respond quickly to changes in forcing. In the Merrimack, tidal time scales dominate and estuarine conditions reflect the present forcing rather than prior conditions in the estuary. This is in sharp contrast with longer, partially mixed systems, where the response time can be much longer than the discharge event time scale or the spring-neap cycle. In the Hudson the length of the salinity intrusion lags the changes in forcing by several days, and during moderate to low discharge periods the estuary responds more slowly than the spring/neap changes in tidal forcing [*Lerczak et al.*, 2009].

[63] The Merrimack (except for low-Q_r cases) equilibrates to changes in forcing in just a few tidal cycles, so modeling of equilibrium conditions is relatively inexpensive computationally. However, the strong along-channel and across-channel gradients in velocity and salinity mean that computational resources must be allocated instead to resolving bathymetry. The flexible resolution of the unstructured finite-volume grid is well suited to these estuaries. Comparing with observations, we found that the bathymetry in our initial model grid was underresolved in regions with sharp gradients at sills and the edges of channels. We collected more bathymetry data in 2007, particularly near the sill, expansion, and channel-shoal transition 4 km west of the mouth. A revised grid incorporated the additional data and increased the model skill, in part because this transition is a region of intense turbulent mixing.

[64] Similarly, we found that the model skill was sensitive to the background diffusivities. The sharp vertical and horizontal salinity gradients were subject to nonphysical mixing when the background diffusivity in the turbulence closure and the sub-grid-scale horizontal diffusivity were high. Skill improved when background vertical diffusivity was set to 10^{-7} m^2 s^{-1} and horizontal diffusivity was set to 0. Even with the low background diffusivity and improved

bathymetry, the model produced too much mixing during flood tides (as shown in the along-channel profiles during the late flood; Figure 5, plots 3 and 4). The leading edge of the salinity front became too diffuse compared with the observations as it traveled up the narrow channel over a series of sills. Excess mixing during flood tides resulted in thicker haloclines and saltier surface layers during ebbs at the up-estuary cross section than seen in the field. The up-estuary bathymetry is insufficiently resolved in the available data, and improvements to the model likely depend on both a finer grid size and more bathymetric data in this region.

[65] Model skills were sensitive to the bathymetry and background diffusivity, but the results were relatively insensitive to the turbulence closure scheme. We have focused on simulations using the $k - \varepsilon$ closure with stability parameters from *Canuto et al.* [2000], but we also tested $k - \varepsilon$ with alternative stability parameters [*Kantha and Clayson*, 1994] and the Mellor-Yamada 2.5 closure [*Mellor and Yamada*, 1982]. Despite the strong vertical salinity gradients, the model skills remained insensitive to the turbulent closure as long as the background diffusivity was sufficiently small. The closures produced somewhat different results, but the variability among them could not be distinguished from the observations. Similarly, simulations with realistic wind forcing had only moderate effects on the results, improving model skill slightly. Strong winds modified the salinity of water advecting into the estuary during flood tides by enhancing mixing of the plume near the liftoff at the mouth bar. Flood tides after ebbs with strong winds were slightly fresher (typically 1–2 psu) than during similar calm wind conditions.

6. Summary

[66] Using field observations and numerical simulations we document conditions and salt flux mechanisms in an estuary where fluvial and tidal forcing are strong and the baroclinic circulation is comparatively weak. Several characteristics distinguish the Merrimack River and similar estuaries from deeper, more weakly forced systems where baroclinic exchange is dominant. At moderate to high discharge the Merrimack is highly variable at tidal time scales. A bottom salinity front at the mouth bar creates strong stratification that persists until mid ebb, and a tidal intrusion front moves into the estuary each tide. During the ebbs the bottom salinity front retreats through a series of sills and expansions where the longitudinal salinity gradient intensifies until mixing and advection push it down-estuary.

[67] The salt flux in the Merrimack is predominantly due to tidal processes rather than steady shear from baroclinic or lateral bathymetric gradients. Tidal pumping is important through the narrow constriction of the mouth, but inside the estuary the salt flux is due to tidal asymmetries in the elevation and thickness of the halocline. Unlike scaling for other tidal salt flux mechanisms that depend only on tidal amplitude, the halocline asymmetry depends on both river discharge and tidal velocity. The salinity intrusion length and stratification in the Merrimack vary more with event-to-seasonal shifts in river velocity than with spring-neap changes in tidal amplitude. The estuary shifts from a short, highly stratified system at moderate to high discharge to a longer, more moderately stratified estuary at lower dis-

charges, around when the length of the salinity intrusion is similar to the tidal excursion.

[68] The hydrodynamic model FVCOM achieves high skill in comparison with observations in the Merrimack. The model reproduces not only the time series of water level, salinity, and velocity at various locations in the estuary, but also the spatial structures of salinity, velocity, and salt flux observed in along- and across-estuary transects. Important attributes of the model were relatively accurate and well-resolved bathymetry and low background diffusivities.

References

Allen, J., P. Somerfield, and F. Gilbert (2007), Quantifying uncertainty in high-resolution coupled hydrodynamic-ecosystem models, *J. Mar. Syst.*, 64(1–4), 3–14, doi:10.1016/j.jmarsys.2006.02.010.

Banas, N. S., B. M. Hickey, P. MacCready, and J. A. Newton (2004), Dynamics of Willapa Bay, Washington: A highly unsteady, partially mixed estuary, *J. Phys. Oceanogr.*, 34(11), 2413–2427, doi:10.1175/JPO2637.1.

Bowen, M. M., and W. R. Geyer (2003), Salt transport and the time-dependent salt balance of a partially stratified estuary, *J. Geophys. Res.*, 108(C5), 3158, doi:10.1029/2001JC001231.

Canuto, V. M., A. Howard, Y. Cheng, and M. S. Dubovikov (2001), Ocean turbulence. Part I: One-point closure model—Momentum and heat vertical diffusivities, *J. Phys. Oceanogr.*, 31(6), 1413–1426, doi:10.1175/1520-0485(2001)031<1413:OTPIOP>2.0.CO;2.

Chant, R. J. (2002), Secondary circulation in a region of flow curvature: Relationship with tidal forcing and river discharge, *J. Geophys. Res.*, 107(C9), 3131, doi:10.1029/2001JC001082.

Chen, C., H. Liu, and R. C. Beardsley (2003), An unstructured grid, finite-volume, three-dimensional, primitive equations ocean model: Application to coastal ocean and estuaries, *J. Atmos. Oceanic Technol.*, 20(1), 159–186, doi:10.1175/1520-0426(2003)020<0159:AUGFVT>2.0.CO;2.

Chen, C., J. Qi, C. Li, R. C. Beardsley, H. Lin, R. Walker, and K. Gates (2008), Complexity of the flooding/drying process in an estuarine tidal-creek salt-marsh system: An application of FVCOM, *J. Geophys. Res.*, 113, C07052, doi:10.1029/2007JC004328.

Eggleston, D., D. Armstrong, W. Elis, and W. Patton (1998), Estuarine fronts as conduits for larval transport: Hydrodynamics and spatial distribution of Dungeness crab postlarvae, *Mar. Ecol. Prog. Ser.*, 164, 73–82, doi:10.3354/meps164073.

Fischer, H. (1972), Mass transport mechanisms in partially stratified estuaries, *J. Fluid Mech.*, 53(4), 671–687, doi:10.1017/S0022112072000412.

Fischer, H. B., E. J. List, R. C. Y. Koh, J. Imberger, and N. H. Brooks (1979), *Mixing in Inland and Coastal Waters*, Academic Press, San Diego, Calif.

FitzGerald, D. M., I. V. Buynevich, R. A. Davis, and M. S. Fenster (2002), New England tidal inlets with special reference to riverine-associated inlet systems, *Geomorphology*, 48(1–3), 179–208, doi:10.1016/S0169-555X(02)00181-2.

Franks, P. (1992), Sink or swim: Accumulation of biomass at fronts, *Mar. Ecol. Prog. Ser.*, 82(1), 1–12, doi:10.3354/meps082001.

Friedrichs, M. A. M., et al. (2007), Assessment of skill and portability in regional marine biogeochemical models: Role of multiple planktonic groups, *J. Geophys. Res.*, 112, C08001, doi:10.1029/2006JC003852.

Garvine, R. W. (1975), The distribution of salinity and temperature in the Connecticut River estuary, *J. Geophys. Res.*, 80(9), 1176–1183, doi:10.1029/JC080i009p01176.

Garvine, R. W., R. K. McCarthy, and K. Wong (1992), The axial salinity distribution in the delaware estuary and its weak response to river discharge, *Estuarine Coastal Shelf Sci.*, 35(2), 157–165, doi:10.1016/S0272-7714(05)80110-6.

Geyer, W. R. (1993), Three-dimensional tidal flow around headlands, *J. Geophys. Res.*, 98(C1), 955–966, doi:10.1029/92JC02270.

Geyer, W. R., and D. M. Farmer (1989), Tide-induced variation of the dynamics of a salt wedge estuary, *J. Phys. Oceanogr.*, 19(8), 1060–1072, doi:10.1175/1520-0485(1989)019<1060:TIVOTD>2.0.CO;2.

Geyer, W. R., and H. M. Nepf (1996), Tidal pumping of salt in a moderately stratified estuary, in *Buoyancy Effects on Coastal and Estuarine Dynamics*, *Coastal and Estuarine Studies*, vol. 53, edited by D. G. Aubrey and C. T. Friedrichs, pp. 213–226, AGU, Washington, D.C.

Geyer, W. R., and R. P. Signell (1992), A reassessment of the role of tidal dispersion in estuaries and bays, *Estuaries*, 15(2), 97–108, doi:10.2307/1352684.

Hansen, D. V., and M. Rattray (1966), New dimensions in estuary classification, *Limnol. Oceanogr.*, 11(3), 319–326.

Hartwell, A. D. (1970), *Hydrography and Holocene Sedimentation of the Merrimack River Estuary, Massachusetts*, Contrib. No. 5, Coastal Research Center, Univ. of Massachusetts, Amherst.

Hughes, F., and J. Rattray (1980), Salt flux and mixing in the Columbia River Estuary, *Estuarine Coastal Mar. Sci.*, 10(5), 479–493, doi:10.1016/S0302-3524(80)80070-3.

Hunkins, K. (1981), Salt dispersion in the Hudson Estuary, *J. Phys. Oceanogr.*, 11(5), 729–738, doi:10.1175/1520-0485(1981)011<0729:SDITHE>2.0.CO;2.

Ibanez, C., D. Pont, and N. Prat (1997), Characterization of the Ebre and Rhone estuaries: A basis for defining and classifying salt-wedge estuaries, *Limnol. Oceanogr.*, 42(1), 89–101.

Jay, D. A., and J. D. Smith (1990a), Residual circulation in shallow estuaries 1. Highly stratified, narrow estuaries, *J. Geophys. Res.*, 95(C1), 711–731, doi:10.1029/JC095iC01p00711.

Jay, D. A., and J. D. Smith (1990b), Circulation, density distribution and neap-spring transitions in the Columbia River estuary, *Prog. Oceanogr.*, 25(1–4), 81–112, doi:10.1016/0079-6611(90)90004-L.

Kalkwijk, J., and R. Booij (1986), Adaptation of secondary flow in nearly horizontal flow, *J. Hydraul. Res.*, 24(1), 19–37.

Kantha, L. H., and C. A. Clayson (1994), An improved mixed layer model for geophysical applications, *J. Geophys. Res.*, 99(C12), 25,235–25,266.

Kay, D. J., D. J. Jay, and J. D. Musiak (1996), Salt transport calculations from acoustic Doppler current profiler (ADCP) and conductivity-temperature-depth (CTD) data: A methodological study, in *Buoyancy Effects on Coastal and Estuarine Dynamics*, *Coastal and Estuarine Studies*, vol. 53, edited by D. G. Aubrey and C. T. Friedrichs, pp. 195–212, AGU, Washington, D.C.

Keulegan, G. (1966), The mechanism of an arrested saline wedge, in *Estuary and Coastline Hydrodynamics*, edited by A. Ippen, pp. 546–574, McGraw-Hill, New York.

Kranenburg, C. (1986), A time scale for long-term salt intrusion in well-mixed estuaries, *J. Phys. Oceanogr.*, 16(7), 1329–1331, doi:10.1175/1520-0485(1986)016<1329:ATSFLT>2.0.CO;2.

Largier, J. (1992), Tidal intrusion fronts, *Estuaries Coasts*, 15(1), 26–39, doi:10.2307/1352707.

Lerczak, J. A., W. R. Geyer, and R. J. Chant (2006), Mechanisms driving the time-dependent salt flux in a partially stratified estuary, *J. Phys. Oceanogr.*, 36(12), 2296–2311, doi:10.1175/JPO2959.1.

Lerczak, J. A., W. R. Geyer, and D. K. Ralston (2009), The temporal response of the length of a partially stratified Estuary to changes in river flow and tidal amplitude, *J. Phys. Oceanogr.*, 39(4), 915–933, doi:10.1175/2008JPO3933.1.

Li, M., L. Zhong, and W. C. Boicourt (2005), Simulations of Chesapeake Bay estuary: Sensitivity to turbulence mixing parameterizations and comparison with observations, *J. Geophys. Res.*, 110, C12004, doi:10.1029/2004JC002585.

MacCready, P. (1999), Estuarine adjustment to changes in river flow and tidal mixing, *J. Phys. Oceanogr.*, 29(4), 708–726, doi:10.1175/1520-0485(1999)029<0708:EATCIR>2.0.CO;2.

MacCready, P. (2007), Estuarine adjustment, *J. Phys. Oceanogr.*, 37(8), 2133–2145, doi:10.1175/JPO3082.1.

Mellor, G. L., and T. Yamada (1982), Development of a turbulence closure model for geophysical fluid problems, *Rev. Geophys. Space Phys.*, 20, 851–875, doi:10.1029/RG020i004p00851.

Mendes, S., W. Turrell, T. Lütkebohle, and P. Thompson (2002), Influence of the tidal cycle and a tidal intrusion front on the spatio-temporal distribution of coastal bottlenose dolphins, *Mar. Ecol. Prog. Ser.*, 239, 221–229, doi:10.3354/meps239221.

Monismith, S. G., W. Kimmerer, J. R. Burau, and M. T. Stacey (2002), Structure and flow-induced variability of the subtidal salinity field in northern San Francisco Bay, *J. Phys. Oceanogr.*, 32(11), 3003–3019, doi:10.1175/1520-0485(2002)032<3003:SAFIVO>2.0.CO;2.

Murphy, A. H. (1988), Skill scores based on the mean square error and their relationships to the correlation coefficient, *Mon. Weather Rev.*, 116(12), 2417–2424, doi:10.1175/1520-0493(1988)116<2417:SSBOTM>2.0.CO;2.

Nunes, R. A., and J. H. Simpson (1985), Axial convergence in a well-mixed estuary, *Estuarine Coastal Shelf Sci.*, 20(5), 637–649, doi:10.1016/0272-7714(85)90112-X.

Oke, P. R., J. S. Allen, R. N. Miller, G. D. Egbert, J. A. Austin, J. A. Barth, T. J. Boyd, P. M. Kosro, and M. D. Levine (2002), A modeling study of the three-dimensional continental shelf circulation off Oregon, Part I: Model–data comparisons, *J. Phys. Oceanogr.*, *32*(5), 1360–1382, doi:10.1175/1520-0485(2002)032<1360:AMSOTT>2.0.CO;2.

Okubo, A. (1973), Effect of shoreline irregularities on streamwise dispersion in estuaries and other embayments, *Neth. J. Sea Res.*, *6*(1/2), 213–224, doi:10.1016/0077-7579(73)90014-8.

Pritchard, D. (1952), Salinity distribution and circulation in the Chesapeake Bay estuarine system, *J. Mar. Res.*, *11*(2), 106–123.

Ralston, D. K., and M. T. Stacey (2007), Tidal and meteorological forcing of sediment transport in tributary mudflat channels, *Cont. Shelf Res.*, *27*(10/11), 1510–1527, doi:10.1016/j.csr.2007.01.010.

Rodi, W. (1987), Examples of calculation methods for flow and mixing in stratified fluids, *J. Geophys. Res.*, *92*(C5), 5305–5328, doi:10.1029/JC092iC05p05305.

Seim, H. E., and M. C. Gregg (1997), The importance of aspiration and channel curvature in producing strong vertical mixing over a sill, *J. Geophys. Res.*, *102*(C2), 3451–3472, doi:10.1029/96JC03415.

Simpson, J., J. Brown, J. Matthews, and G. Allen (1990), Tidal straining, density currents, and stirring in the control of estuarine stratification, *Estuaries*, *13*(2), 125–132, doi:10.2307/1351581.

Stacey, M. T., and D. K. Ralston (2005), The scaling and structure of the estuarine bottom boundary layer, *J. Phys. Oceanogr.*, *35*(1), 55–71, doi:10.1175/JPO-2672.1.

Stacey, M. T., J. R. Burau, and S. G. Monismith (2001), Creation of residual flows in a partially stratified estuary, *J. Geophys. Res.*, *106*(C8), 17,013–17,037.

Stommel, H., and H. Farmer (1952), *On the Nature of Estuarine Circulation*, Woods Hole Oceanographic Institution, Woods Hole, Mass.

Umlauf, L., and H. Burchard (2003), A generic length-scale equation for geophysical turbulence models, *J. Mar. Res.*, *61*, 235–265, doi:10.1357/002224003322005087.

Uncles, R. J., and J. A. Stephens (1996), Salt intrusion in the tweed estuary, *Estuarine Coastal Shelf Sci.*, *43*(3), 271–293, doi:10.1006/ecss.1996.0070.

Wang, B., O. Fringer, S. Giddings, and D. Fong (2009), High-resolution simulations of a macrotidal estuary using SUNTANS, *Ocean Model.*, *26*(1/2), 60–85, doi:10.1016/j.ocemod.2008.08.006.

Warner, J. C., W. R. Geyer, and J. A. Lerczak (2005), Numerical modeling of an estuary: A comprehensive skill assessment, *J. Geophys. Res.*, *110*, C05001, doi:10.1029/2004JC002691.

Wilmott, C. (1981), On the validation of models, *Phys. Geogr.*, *2*, 184–194.

Zimmerman, J. (1986), The tidal whirlpool: A review of horizontal dispersion by tidal and residual currents, *Neth. J. Sea Res.*, *20*(2/3), 133–154, doi:10.1016/0077-7579(86)90037-2.

W. R. Geyer and D. K. Ralston (corresponding author), Applied Ocean Physics and Engineering, MS 11, Woods Hole Oceanographic Institution, Woods Hole, MA 02540, USA. (dralston@whoi.edu)

J. A. Lerczak, College of Oceanic and Atmospheric Sciences, Oregon State University, Corvallis, OR 97331, USA.